Bioactive Materials 39 (2024) 354–374

Contents lists available at ScienceDirect

Bioactive Materials

journal homepage: www.keaipublishing.com/en/journals/bioactive-materials

Fluffy hybrid nanoadjuvants for reversing the imbalance of osteoclastic and osteogenic niches in osteoporosis

Guoyang Zhang [a,b,f,g,1], Yuhao Kang [a,b,f,g,1], Jizhao Dong [c,1], Dingyi Shi [b,f], Yu Xiang [a,b,g], Haihan Gao [a,b,g], Zhiqi Lin [a,b,g], Xiaojuan Wei [a,g], Ren Ding [d], Beibei Fan [e,**], Hongmei Zhang [c], Tonghe Zhu [c,***], Liren Wang [a,b,f,g,****], Xiaoyu Yan [a,b,g,*]

[a] Shanghai Sixth People's Hospital Affiliated to Shanghai Jiao Tong University School of Medicine, No. 600 Yishan Road, Shanghai, 200233, China
[b] Shanghai Jiao Tong University School of Medicine, No. 227 South Chongqing Road, Shanghai, 200025, China
[c] Multidisciplinary Centre for Advanced Materials, Institute for Frontier Medical Technology, School of Chemistry and Chemical Engineering, Shanghai University of Engineering Science, No.333 Longteng Road, Shanghai, 201620, China
[d] Shanghai Baoshan District Hospital of Integrated Traditional Chinese and Western Medicine, Department of Orthopedics, No. 181 Youyi Road, Shanghai, 201900, China
[e] Shanghai Baoshan District Hospital of Integrated Traditional Chinese and Western Medicine, Department of Pharmacy, No. 181 Youyi Road, Shanghai, 201900, China
[f] Regenerative Sports Medicine and Translational Youth Science and Technology Innovation Workroom, Shanghai Jiao Tong University School of Medicine, No. 227 South Chongqing Road, Shanghai, 200025, China
[g] Regenerative Sports Medicine Lab of the Institute of Microsurgery on Extremities, Shanghai Sixth People's Hospital Affiliated to Shanghai Jiao Tong University School of Medicine, No. 600 Yishan Road, Shanghai, 200233, China

ARTICLE INFO

Keywords:
Osteoporosis
nanoadjuvants
topological morphology
bone niches
Adhesion

ABSTRACT

Osteoporosis is majorly caused by an imbalance between osteoclastic and osteogenic niches. Despite the development of nationally recognized first-line anti-osteoporosis drugs, including alendronate (AL), their low bioavailability, poor uptake rate, and dose-related side effects present significant challenges in treatment. This calls for an urgent need for more effective bone-affinity drug delivery systems. In this study, we produced hybrid structures with bioactive components and stable fluffy topological morphology by cross-linking calcium and phosphorus precursors based on mesoporous silica to fabricate nanoadjuvants for AL delivery. The subsequent grafting of -PEG-$DAsp_8$ ensured superior biocompatibility and bone targeting capacity. RNA sequencing revealed that these fluffy nanoadjuvants effectively activated adhesion pathways through CARD11 and CD34 molecular mechanisms, hence promoting cellular uptake and intracellular delivery of AL. Experiments showed that small-dose AL nanoadjuvants effectively suppress osteoclast formation and potentially promote osteogenesis. *In vivo* results restored the balance between osteogenic and osteoclastic niches against osteoporosis as well as the consequent significant recovery of bone mass. Therefore, this study constructed a drug nanoadjuvant with peculiar topological structures and high bone targeting capacities, efficient intracellular drug delivery as well as bone bioactivity. This provides a novel perspective on drug delivery for osteoporosis and treatment strategies for other bone diseases.

Peer review under responsibility of KeAi Communications Co., Ltd.

* Corresponding authors. Shanghai Sixth People's Hospital Affiliated to Shanghai Jiao Tong University School of Medicine, No. 600 Yishan Road, Shanghai, 200233, China.

** Corresponding author. Shanghai Baoshan District Hospital of Integrated Traditional Chinese and Western Medicine, Department of Pharmacy, No. 181 Youyi Road, Shanghai, 201900, China.

*** Corresponding author. Multidisciplinary Centre for Advanced Materials, Institute for Frontier Medical Technology, School of Chemistry and Chemical Engineering, Shanghai University of Engineering Science, No.333 Longteng Road, Shanghai, 201620, China.

**** Corresponding author. Shanghai Sixth People's Hospital Affiliated to Shanghai Jiao Tong University School of Medicine, No. 600 Yishan Road, Shanghai, 200233, China.

E-mail addresses: jessiefan2012@163.com (B. Fan), zhutonghe89@sues.edu.cn (T. Zhu), wangliren13@163.com (L. Wang), xyyan@sjtu.edu.cn (X. Yan).

[1] Guoyang Zhang, Yuhao Kang, and Jizhao Dong have contributed equally to this work and they are the co-first authors of the article.

https://doi.org/10.1016/j.bioactmat.2024.05.037
Received 22 February 2024; Received in revised form 4 May 2024; Accepted 20 May 2024

1. Introduction

Osteoporosis is a common bone disease that affects over 200 million individuals globally with a prevalence rate of 18.3 % [1–3]. It is primarily caused by an imbalance between the osteoclastic and osteogenic niches. The excessive osteoclast activity and reduced osteogenesis cause decreased bone mass, bone microstructure deterioration, and increased susceptibility to fractures. The cost of treatment of osteoporosis and its associated fragility fractures present a substantial challenge to public health and government economies [4,5]. Several anti-osteoporosis drugs have been developed, among which Alendronate (AL) is a third-generation bisphosphonate and an internationally recognized first-line treatment [6–8]. Nevertheless, their clinical applications have been restricted due to poor absorption after oral administration, low uptake efficiency, and limited bioavailability arising from systemic distribution before reaching the target site [9,10]. Consequently, long-term administration at high doses is often required to achieve therapeutic effects. Although AL may inhibit osteogenesis, it causes adverse reactions including gastrointestinal toxicity, mandibular osteonecrosis, atypical fractures, and other problems [11–15]. Therefore, there is an urgent need to develop more effective drug delivery systems with enhanced affinity towards bones (see Scheme 1).

To achieve the therapeutic efficacy of drugs while minimizing side effects, it is important to improve the drug-delivering efficiency and uptake rate, prevent clearance by the mononuclear phagocyte system, as well as reduce application dosage. In recent years, mesoporous silica nanoparticles have gained significant attention due to their high specific surface area and pore volume. These characteristics allow for significant drug loading, while simultaneously maintaining controlled release kinetics. This extends the *in vivo* half-life of the drug, potentially reducing the need for long-term high dosage administration [16–19]. Furthermore, these nanoparticles have excellent biocompatibility and are amenable to surface modifications, rendering them suitable for drug nanoadjuvants [20–25]. Nonetheless, their applications in drug delivery still face major challenges due to insufficient biological activity, poor endocytosis efficiency, and simple biological function due to a lack of bioactive ingredients and their basic structures. Thus, additional studies are essential to investigate the design of their chemical components and structural modification [26].

Recent studies have shown that the unique surface morphology of nanomaterials can significantly improve their intracellular uptake capacity. Moreover, nanospikes can manipulate the recruitment of myosin IIA on the cell membrane during cellular uptake, thereby improving absorption efficiency [27]. Additionally, virus-mimicking nano-surfaces promote biomolecule binding and subsequently increase cellular uptake. This mechanism may leverage the natural interaction between viruses and host cells [28]. Furthermore, these mesoporous silica nanoparticles with unique surface morphology act as nanoadjuvants in tumor treatment to induce apoptosis and necrosis of tumor tissue after drug delivery. However, limited studies have been conducted on osteoporosis and orthopedic disease therapies, specifically for promoting osteogenesis and bone regeneration [29–33]. Inspired by previous research and the special phenomenon that fluffy and prickly balls can easily adhere and be absorbed by cells, we hypothesized that incorporating bioactive chemical components and designing unique morphological structures could effectively enhance the intracellular delivery

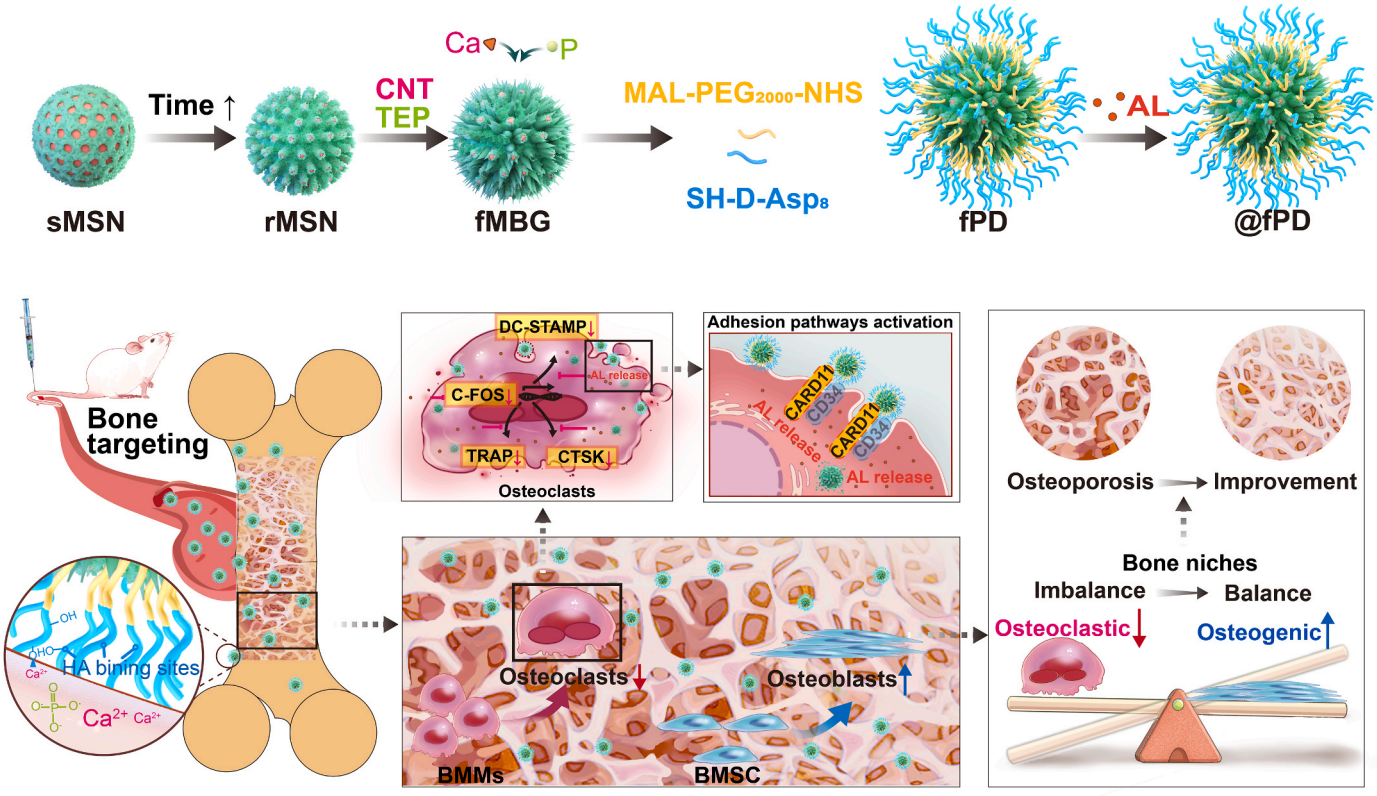

Scheme 1. Fluffy hybrid nanoadjuvants for restoring osteoclastic and osteogenic balance in osteoporosis. sMSN, smooth mesoporous silica nanoparticles. rMSN, rough mesoporous silica nanoparticles. fMBG, fluffy mesoporous bioactive-glass-like nanoparticles. CNT, $Ca(NO_3)_2{\cdot}4H_2O$. TEP, triethyl phosphate. Ca, calcium element. P, phosphorus element. MAL-PEG_{2000}-NHS, Maleimide-$Pegyl_{2000}$-NHS ester. SH-D-Asp_8, mercapto-dextro-aspartate octapeptide. fPD, fluffy bone targeting mesoporous bioactive-glass-like nanoparticles. AL, Alendronate. @fPD, fluffy bone targeting mesoporous bioactive-glass-like AL nanoadjuvants. HA, hydroxyapatite. BMMs, bone marrow-derived macrophages. M-CSF, macrophage colony-stimulating factor. RANKL, Nuclear factor kappa B receptor activator ligand. CARD11, caspase recruitment domain 11. CD34, differentiation antigen cluster 34. C-FOS, Fos proto-oncogene. CTSK, cathepsin K. TRAP, tartrate-resistant acid phosphatase. DC-STAMP, dendritic cells express seven transmembrane proteins. BMSC, bone marrow mesenchymal stem cells. OCs, osteoclasts. OBs, osteoblasts.

efficiency and biological function of nanoadjuvants in orthopedic disease treatments.

A unique topologically fluffy mesoporous bioactive nanoadjuvant (fMBG) was synthesized by incorporating $Ca(NO_3)_2{\cdot}4H_2O$ (CNT) and triethyl phosphate (TEP) into silica nanoparticles. Through the synergistic action and cross-linking of Si, O, Ca, and P systems, fluffy topological surface structures were formed and developed by changing a simple Si–O network supported by the oil-water biaxial epitaxial growth technique. fMBG was further integrated with -PEG-$DAsp_8$ as fPD to improve biocompatibility and bone targeting. Subsequently, nanoadjuvants @fPD were prepared by encapsulating with AL. The @fPD had excellent bioactivity, biocompatibility, bone targeting capacity, and high treatment efficiency at lower AL dosage. RNA sequencing revealed that @fPD significantly improved uptake rate and intracellular delivery by activating adhesion pathways involving CARD11 and CD34 molecule mechanisms. Both *in vitro* and *in vivo* experiments showed that @fPD effectively restores the balance of osteoclastic-osteogenic niches. It also promotes bone formation by significantly suppressing the osteoclastic activity of bone marrow-derived monocytes (BMMs) while potentially boosting the osteogenic capacity of bone marrow mesenchymal stem cells (BMSC). This work constructs a topologically fluffy bioactive drug nanoadjuvant with increased uptake rate and intracellular delivery while providing a new perspective for developing drug treatments for osteoporosis and other bone diseases.

2. Experimental section/Methods

2.1. Materials

Hexadecyltrimethylammonium bromide (CTAB), alendronate (AL), and ninhydrin was purchased from Sigma-Aldrich. Tetraethylorthosilicate (TEOS), triethyl phosphate (TEP) and cyclohexane were bought from Shanghai Adamas Reagent Co., Ltd. Sodium hydroxide (NaOH), sodium bicarbonate ($NaHCO_3$), calcium nitrate tetrahydrate (CNT, $Ca(NO_3)_2{\cdot}4H_2O$), ethanol and methyl alcohol were purchased from Shanghai Chemical Co., Ltd. (3-Aminopropyl) triethoxysilane (APTES) were procured from Aladdin Industrial Inc. PBS and SBF with different pH values were obtained from Shanghai yuanye Bio-Technology Co., Ltd. Maleimide-PEG_{2000}-NHS ester (MAL-PEG_{2000}-NHS) and dextrorotation aspartic octapeptide (D-Asp_8-SH) from Guangzhou Tanshui Technology Co. Ltd. (Guangzhou, China). Fluoresceine isothiocyanate (FITC) was purchased from XI'AN QIYUE BIOLOGY Co. Ltd. Ultra-pure water with a resistivity of 18.2MΩ•cm was used throughout the experiment.

2.2. Preparation of sMSN, rMSN and fMBG

1.0g CTAB and 0.8 mL NaOH (0.1 M) were added to 50 mL deionized water, stirred gently at a 60 °C circular bottom for 2 h. Next, 20 mL (20 % v/v) TEOS solution of cyclohexane was added to the mixture. If stirred at 60 °C at 120 rpm for 24 h, smooth mesoporous silica nanoparticles sMSN were obtained. The rough mesoporous silica nanoparticles rMSN were prepared by stirring at 30 rpm for 48 h under the same reaction temperature. The preparation procedure of fluffy mesoporous silica nanoparticles fMBG was similar to that of rough mesoporous silica nanoparticles. The difference was that after addition of 20 mL (20 % v/v) TEOS cyclohexane solution, 0.298 g (0.28 mL) triethyl phosphate was added to the above solution after stirring at 60 °C for 30 min. It was further stirred for 30 min to ensure complete and uniform mixing, and 2.318 g $Ca(NO_3)_2{\cdot}4H_2O$ was added, and stirred at 30 rpm for 48 h. This was followed by centrifugation to collect the pellet that was washed with water and ethanol several times. Subsequently, the dried nanoparticles were heated at 5 °C/min and reacted in Muffle furnace at 550 °C for 6 h to remove the CTAB template. Finally, the samples were washed with ethanol and deionized water and dried under vacuum at 45 °C for 8 h.

2.3. The mesoporous nanoparticles were functionalized to obtain @sPD, @rPD and @fPD

2.3.1. Amination modification

50 mg nanoparticles were activated by vacuum drying for 2h at 110 °C, mixed with 10 mL 99 % ethanol solution and ultrasonically dispersed. They were then mixed with 25 μL APTES solution, condensed under nitrogen protection at 70 °C for reflux for 6 h. It was then centrifuged and the resultant white products were collected, washed three times with ethanol, dried and preserved.

2.3.2. Bone targeting modification

10 mg each of the aminated mesoporous nanoparticles was dispersed in 5 mL PBS to obtain liquid A, dissolve 0.018 mmol MAL-PEG_{2000}-NHS in 5 mL PBS to obtain liquid B. Liquid A and B were mixed and stirred under the protection of nitrogen at room temperature in the dark for 1 h. 0.028 mmol D-Asp_8-SH solution dissolved in 10 mL PBS was then added into the solution, and centrifuged. The resulting products were washed with PBS, stirred under the protection of nitrogen at room temperature in darkness for 24 h, and lyophilized to obtain sPD, rPD and fPD, respectively.

2.3.3. Determination of AL loading and release

The prepared PEG-D-Asp_8-targeted and modified mesoporous nanoparticles were ultrasonically dispersed in 15 mL PBS, from which 5 mL PBS were dissolved in 10 mg AL and mixed. The reaction was performed at room temperature for 24 h in the dark. The products were centrifuged and washed with PBS, and the supernatant and PBS washing solution were collected. The final products @sPD, @rPD and @fPD were collected after precipitation and lyophilization. The drug loading of AL was calculated depending on the ninhydrin color reaction method that was described in previous studies, and the precipitates were lyophilized and stored at −20 °C. Briefly, the AL standard stock solution with different equal gradient concentrations and the above-mentioned drug loading supernatant and washing solution after dilution to a series of 10 mL volume bottles, in which 0.5 mL aqueous solution of 0.05 mol/L sodium bicarbonate and 2.5 mL methanol solution of 0.2 % ninhydrin are added. The mixture was heated in a water bath at 90 ± 5 °C for 20 min and then allowed to cool. Deionized water was used to prepare equal volume reach the mark, measure the absorbance at 568 nm, draw a standard curve, and compare the sample concentration. For the release of AL, nanoadjuvants 20 mg loaded with AL were evenly dispersed in 10 mL PBS with pH levels at 7.4 or 6.0, respectively, at a temperature of 37 °C. After the preset duration, 2 mL of the medium was extracted from the release buffer. The same method was employed to quantify the release at several time intervals including 10 min, 30 min, 60 min, 2 h, 4 h, 6 h, 24 h, and 48 h.

2.3.4. FITC fluorophore modification

10 mg each of the prepared mesoporous nanoparticles were dispersed in 5 mL ethanol and 0.5 mg fluorescein isothiocyanate (FITC) was added. The mixture was stirred in darkness for 24 h. The product was then centrifuged and washed with ethanol. It was vacuum dried at 45 °C to obtain the target product.

2.4. In vitro cytology experiments

2.4.1. Cell culture

The human bone marrow mesenchymal stem cells (BMSC cells, Oricell, HUXMA-01001) were induced to differentiate into osteoblasts (OBs). In addition, mouse bone marrow-derived macrophages (BMMs) were induced to differentiate into osteoclast (OCs) (Vitonlihua Company). They were then cultured in the minimum essential medium α (Alpha-MEM, Gibco), containing10 % fetal bovine serum (FBS, Oricell), and 1 % penicillin-streptomycin - amphotericin B (Beyotime). Mouse mononocytic macrophage leukemia cells (raw264.7 cells, Shanghai

Institute of Cell Research, Chinese Academy of Sciences) were cultured under similar conditions as above except that the base medium was Dulbecco's modified Eagle medium (DMEM, Gibco). The cells were cultured at 37 °C in an incubator with 5%CO_2.

2.4.2. Measurement of cellular uptake rate

Three types of FITC-labeled mesoporous nanoparticle drug carrier systems were mixed at a concentration of 100 μg/mL. They were incubated with the cells, washed with cold PBS for more than three times, and then lyzed with 0.5 % (w/v) sodium dodecyl sulfate (SDS, pH 8.0). The lysates were measured using fluorescence spectrometry for FITC and by Lowry method to measure the protein content. The uptake level was expressed as the amount of FITC-labeled mesoporous nanoparticle drug carrier systems associated with 1.0 mg of cellular protein.

2.4.3. Osteogenic differentiation, intervention, and ALP and ARS staining

2×10^4 BMSC cells per well were seeded in a 24-well plate for osteogenic induction. DMEM medium containing 10%FBS, 1 % antibiotics, 0.1 μM dexamethasone, 50 μM vitamin C and 10 mM β-glycerol phosphate was changed every 3 days. On the 14th day of induction, the cells were fixed in 4%PFA and stained with ALP (alkaline phosphatase) staining kit and ARS (Alizarin Red S) staining on the 21st day of induction. The cells were imaged, 10 % cetylpyridine chloride was added to the cells, and incubated at room temperature for 30 min. Finally, the OD value was read at 562 nm to detect the OD values using the enzymoscope. The OD value was analyzed to determine the ARS.

2.4.4. Osteoclastic differentiation, intervention and TRAP staining

The harvesting and culture of BMMs were performed as previously described. C57BL/6 mice (8 weeks old, male) were euthanized with 4 % pentobarbital sodium, they were immersed in 75 % ethanol for 10 min. The musculature of the hind limb was extracted to obtain the femur and tibia. The long bone was cut to expose the bone marrow cavity. The entire cavity was washed with PBS using a sterile 5 mL syringe. It was centrifuged at 1200 rpm for 3 min, and the supernatant was discarded. Next, 5 mL of red cell lysis buffer was added to the cells and incubated on ice for 10 min to allow cell precipitation. It was then centrifuged and cells were re-suspended in 10 mL alpha-mem complete culture medium and inoculated in 100 mm cell culture dishes for further proliferation. After 24 h, the cells were collected and re-suspended in 10 mL alpha-Mem medium containing 30 ng/mL macrophage colony-stimulating factor (M-CSF, Peprotech) and re-inoculated for 3 days in 100 mm cell culture dishes. The adherent cells at the bottom of the flask were BMMs. The cells were allowed to grow to reach a confluence of 90 % while being digested by trypsin (Gibco) for 15 min. They were then centrifuged to remove supernatant and re-suspended in a α-MEM complete medium containing 30 ng/mL M-CSF and 60 ng/mL NF-κB receptor activator (RANKL, Peprotech). 2×10^5 cells were incubated in 24-well plates and treated with PBS and various concentrations (10, 30, 50, 100 μg/mL) of @sPD, @rPD, and @fPD. For each group, three replicates were prepared. The BMMs groups without M-CSF and RANKL served as the negative controls. On day 5 of induction, 4 % paraformaldehyde (PFA) was added to the cells and incubated at room temperature for 10 min and then maintained with a TRAP kit (Sigma) working solution at 37° for 60 min.

2.4.5. Bone slices

To simulate the effect of bone absorption *in vivo*, freeze-dried bovine bone slices (Φ6 mm x 0.5 mm) were placed at the bottom of a 96-well plate, BMMs (10 x 103/well) were seeded on the surface of the bone slices and incubated for 7 days under the same conditions described above. The bone plates were fixed with 4 % paraformaldehyde (PFA) for 30 min, and the surface cells of the bone plates were collected through ultrasound with 3 % ammonia. The surface of the bone fragments was sprayed with Au–Pd and observed with a scanning electron microscope (JEOL JCM-7000).

2.4.6. RT - qPCR

Total RNA was extracted from cultured target cells using EZ-press RNA Purification Kit and quantify RNA purity and its concentration was determined using NanoDrop 2000 (Thermo Fisher Scientific). gDNA was digested using a 4 × EZscript Reverse Transcription Mix II kit and 1 μg of cDNA for each sample was subjected to Real-time PCR using 2 × Color SYBR Green qPCR Master Mix in CFX96 real-time system (Bio-Rad). The mRNA levels of target genes was calculated using $2^{-\Delta\Delta CT}$ method. Results were normalized to the expression of GAPDH. See Supplemental Materials for primers used in the qPCR.

2.4.7. Cellular immunofluorescence

Cells were cultured on 24-well plate and fixed with 4 % paraformaldehyde at room temperature for 10 min. The cells were permeated with 0.1 % Triton X-100 on PBS at 4 °C for 10 min and osteoclast (OCs) were stained with TRITC Phalloidin (40734ES75, YEASEN, 1:200). This step was omitted due to the membrane composition characteristics of CARD11 and CD34. The cells were incubated with 4%BSA under PBS at 37 °C for 30 min to block non-specific interactions. They were then incubated with primary antibody at 4 °C overnight. The primary antibodies used in this study were as follows: CARD11 (#sc-166910, SCBT, 1:200), CD34 (#sc-74499, SCBT, 1:200). The next day, the cells were rinsed with PBS for 5 min to remove primary antibodies. The cells were then incubated with the corresponding secondary antibody (AB_2338478, Jackson Immuno Research, 1:200) at room temperature for 1 h and then washed three times with PBS. Finally, 500 μL DAPI staining reagent was added to each well and treated at room temperature for 10 min. The fluorescence of cells was recorded and images were obtained using a Leica DMi8 inverted microscope.

2.4.8. Western blot

The cells were treated with IP cell lysis solution (beyotime) to extract proteins on ice. with the protein samples were separated by 4 %–12 % gradient SimplePAGEBis-Tris denaturing gel electrophoresis. This was followed by electrotransfer to 0.22 μm PVDF membrane by wet transfer method and blocked with 5%BSA at room temperature for 1 h. The membrane was incubated at 4 °C with CARD11 (#sc-166910, SCBT, 1:500), CD34 (#sc-74499, SCBT, 1:500) and PKP3 (#sc-166655, SCBT, 1:500), GAPDH (#5174, CST, 1:1000). It was then probed with secondary antibody (#7076, CST, 1:2500) (#ab205718, Abcam, 1:3000) conjugated with horseradish peroxidase (HRP) at room temperature for 1 h. Finally, the antibody-antigen complex was visualized using ECL reagent (Millipore). The uncropped staining image of Primrose is shown in Supplementary Figure 24A.

2.4.9. RNA - seq

Total RNA was extracted from the samples and subjected to agarose gel separation to determine RNA integrity. The extracted RNA was reverse-transcribed to construct cDNA library which was then sequenced on Illumina platform. Bioinformatic analysis of differentially expressed genes (DEGs) was performed using OmicShare Tools. Sequence information is presented in the Supplementary Figure 19-25.

2.5. Animal experiments

2.5.1. Animal feeding

C57BL/6J mice and Sprague-Dawley rats were purchased from Vitonglihua Laboratory Animal Co., LTD. The animals were randomly assigned into groups and housed in a pathogen-free house under 12-h light and 12-h dark cycles. The temperature (23 ± 2 °C) and humidity (55 %) were kept constant, to allow all animals free access to food and clean water. All animal experiments were approved by the Animal Ethics Committee of the Sixth People's Hospital Affiliated to Shanghai Jiao Tong University (Anmal Experiment Registration number No: DWSY2022-0189. Animal Welfare Ethics acceptance number No: DWLL2024-0592).

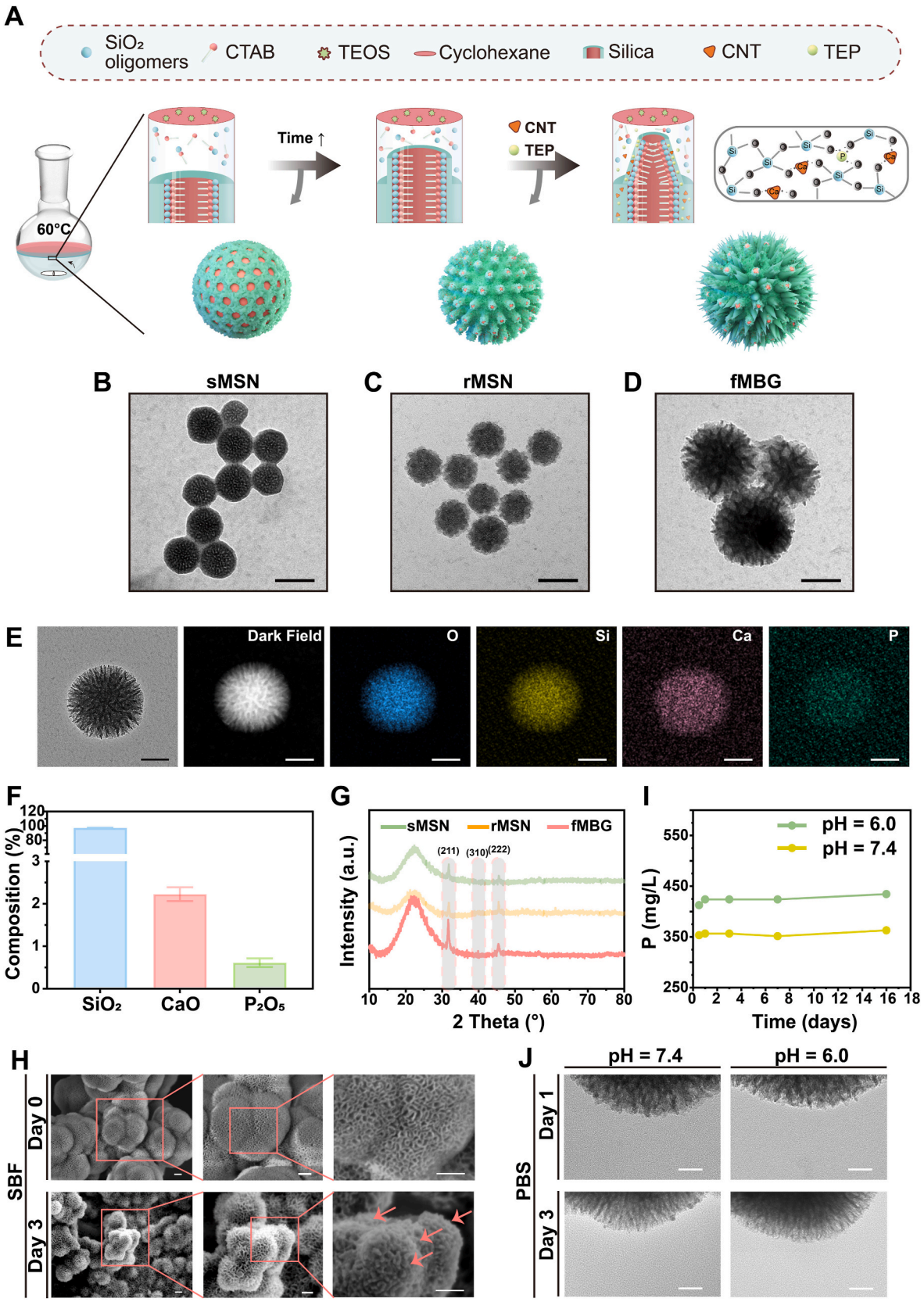

Fig. 1. fMBG has bioactivity and stability *in vitro*. (A) Flow chart showing the synthesis process of smooth mesoporous silica nanoparticles (sMSN), rough mesoporous silica nanoparticles (rMSN), and fluffy mesoporous bioactive-glass-like nanoparticles (fMBG). CNT, $Ca(NO_3)_2{\cdot}4H_2O$. TEP, triethyl phosphate. (B–D) The representative TEM image of sMSN, rMSN and fMBG (scale = 150 nm). (E) Distribution map of elements of fMBG (scale = 150 nm). (F) Quantitative composition of fMBG compounds (n = 5). Data are presented as the mean ± SEM. (G) XRD images of sMSN, rMSN and fMBG soaked for three days in SBF. (H) Representative SEM images corresponding to day 0 and day 3 (scale = 50 nm) of fMBG soaked in SBF for different days. Red arrows indicate the hydroxyapatite (HA) peaks and images. (I and J) Changes in the P content in the soaking PBS at different time points at pH = 7.4 and pH = 6.0 and TEM images corresponding to day 1 and day 3 (scale = 50 nm).

2.5.2. Cyclic experiments

Blood samples were collected from 6–8-week-old rats through eyeballs into tubes containing ethylenediamine tetraacetic acid (EDTA). The blood was centrifuged at 2000 rpm for 5 min, and the supernatant was discarded. The obtained red blood cells were further washed with PBS and 20 μL red blood cells was diluted with 1 mL PBS. The diluted red blood cell suspension (0.2 mL) was mixed with 0.8 mL of different nanoparticles at the concentrations of 25, 50, 100, 200, 300, and 500 μg/mL. PBS and deionized water were used as negative (−) and positive (+) controls, respectively. It was mixed gently by rotating and incubated at room temperature for 1 h. This followed by centrifugation at 2000 rpm for 5 min, the absorbance of the supernatant was determined at 541 nm using an ultraviolet–visible spectrophotometer. The hemolysis rate of red blood cells was calculated as follows. Percentage of hemolysis (%) =(sample absorbance - negative control absorbance)/(positive control absorbance - negative control absorbance) × 100.

2.5.3. Live imaging of small animals

Rats treated with total depilation were anesthetized via intraperitoneal injection of chloral hydrate (4 %, intraperitoneal injection). They were then administered with three types of FITC-grafted mesoporous nanosphere delivery systems (20 mg/kg) via a caudal vein. After injection, the rats were imaged using an IVIS spectrum (PerkinElmer) and specific tissues were isolated 24 h later to quantitatively analyze fluorescence using *in vivo* imaging system (IVIS).

2.5.4. Construction and treatment of ovariectomized rat model of osteoporosis

Female experimental rats aged 6–8 weeks were anesthetized with 2 % pentobarbital sodium injected into the abdomen at the dose of 40 mg/kg body weight. A 1–2 cm incision was made in the side abdomen, and the skin, fascia and muscle were cut or bluntly separated with scissors. Next, pink and bright cauliflower-shaped ovaries were ligated and placed back into the abdominal cavity, and sterilized with penicillin to prevent infection. The osteoporosis model was verified after 12 weeks of feeding on normal diet. The rats were then administered through caudal intravenous route at a dose of 1 mg/kg/2 week in accordance with the nanoadjuvants [34,35].

2.5.5. Micro-CT

To evaluate the microstructure of the distal femur and the L3∼L4 vertebrae as representative sites, samples were scanned using micro-CT (Siemens, Erlangen, Germany) and set as: 8.85 μm isotropic resolution, 450 μA current, 80 kV voltage, 360° rotation for 2000 ms per degree exposure time. Scanning was initiated at 0.5 mm away from the growth plate with a scan slice thickness of 18 μm. 140 cross-sectional long bones and vertebrae were scanned. Three-dimensional (3D) reconstructed bone structure images were collected using CTvox software with a CT threshold of 255. In the 3D reconstruction area, the structural parameters of bone trabeculae and cortical bone were semi-automatically determined using Skyscan, NRecon, Data Viewer, CTAn and Batman software. The following parameters were calculated: bone volume fraction (BV/TV), trabecular thickness (Tb.Th), trabecular number (Tb.N), trabecular separation (Tb.Sp) and cortical bone thickness (T.Ar).

2.5.6. HE staining, TRAP staining and immunohistochemistry

Rat femur and vertebrae samples were immersed in 10%EDTA for decalcification, the solution was changed every 5 days. It was then dehydrated through a series of gradient concentration alcohols, and exposed to xylene solution for clarity. They were the embedded in paraffin wax for 1 h and paraffin blocks were obtained along the long axis of the femur and the maximum sagittal plane of the vertebra. They tissue blocks were stained with hematoxylin and eosin (H&E) kits, TRAP staining kits, and osteocalcin OCN immunohistochemical kits. Positive TRAP staining of polykaryotic cells on the bone surface were considered OCs. Quantification of BV/TV and No.OC/BS was performed using ImageJ software.

2.6. Statistics

Data were expressed as mean ± SEM. Two groups were compared using the unpaired double-tailed student T-test. The Tukey ANOVA post hoc test was performed for one-way ANOVA. Sidak's multiple comparison test was performed for two-way ANOVA. P value < 0.05 was considered statistically significant. *P < 0.05, **P < 0.01, ***P < 0.001, ****P < 0.0001; #P < 0.05, # #P < 0.01, # # #P < 0.001, # # # #P < 0.0001, vs. Control group (default is group 1 in the corresponding experiment). In all groups, data were analyzed from at least three separate experiments.

3. Results

3.1. fMBG has bioactivity and stability in vitro

The synthesis process of fluffy mesoporous bioactive-glass-like nanoparticles (fMBG) is shown in Fig. 1A. Smooth mesoporous silica nanoparticles (sMSN) and rough mesoporous silica nanoparticles (rMSN) act as intermediate products with different surface topological morphology in the synthesis reaction, which were also collected. Fig. 1B–D illustrates the representative transmission electron microscopy (TEM) images of the three nanoparticles. As reported in previous studies [33], the silicon source TEOS underwent hydrolysis in a NaOH alkaline environment, causing the assembly of Si–O network silica nanoparticles. With the extension of the reaction time, the originally relatively smooth mesoporous silica nanoparticles (Fig. 1B) developed numerous protrusions on their surface under the synergistic action of the oil-water biaxial interface of cyclohexane and deionized water, along with the surfactant CTAB; this resulted in a relatively rough morphology (Fig. 1C). When $Ca(NO_3)_2{\cdot}4H_2O$ (CNT) and triethyl phosphate (TEP) were introduced into the system as calcium and phosphorus sources, respectively, the original pure Si–O network structure was further modified to Si, O, Ca, and P cross-link network [36,37], which continually promoted the rough structure growth into fluffy morphology. The particle sizes of the three particles, measured using the Dynamic Light Scattering (DLS) method (Supplementary Figure 1A), were approximately ∼150 nm for sMSN, ∼200 nm for rMSN, and ∼300 nm for fMBG. These findings are consistent with the continuous growth of the structures after the oil-water biaxial epitaxial growth method as well as calcium and phosphorus modification. The nitrogen adsorption results of the three nanoparticles (Supplementary Fig. 2A and B) revealed that the pore volumes of the three nanoparticles successively decreased with surface protrusion growth and doping as well as a modification with calcium and phosphorus. The pore volumes measured by the Barrett-Joyner-Halenda (BJH) method were 0.793 cc/g for sMSN, 0.636 cc/g for rMSN, and 0.481 cc/g for fMBG, respectively. However, the isotherm curves of the three nanoparticles were similar to those of the H1 type with hysteresis, indicating the consistent presence of relatively uniform cylindrical open mesoporous pores. Moreover, there was a decrease in specific surface areas of sMSN (86.244 m^2/g), rMSN (53.581 m^2/g), and fMBG (53.102 m^2/g), also using the Brunauer-Emmett-Teller (BET) method.

The Energy-Dispersive X-ray Spectroscopy (EDS) mapping was used to quantify and analyze the contents of oxygen(O), silicon(Si), calcium (Ca), and phosphorus(P) in fMBG (Fig. 1E and Supplementary Fig. 3A and B). These values differed from the previously reported contents of traditional bioactive glass with 60–90 mol% SiO_2 and 0–40 mol% of CaO and P_2O_5 [36]. The content of SiO_2 in our fluffy mesoporous bioactive-glass-like nanoparticles, fMBG, was 97.16 %, whereas the contents of CaO and P_2O_5 were 2.23 % and 0.61 % (in average form), respectively (Fig. 1F). These values are attributed to our specific feeding sequence, feeding time, and feeding ratio, as our objective was to further modify the surface structure while maintaining the rough topological

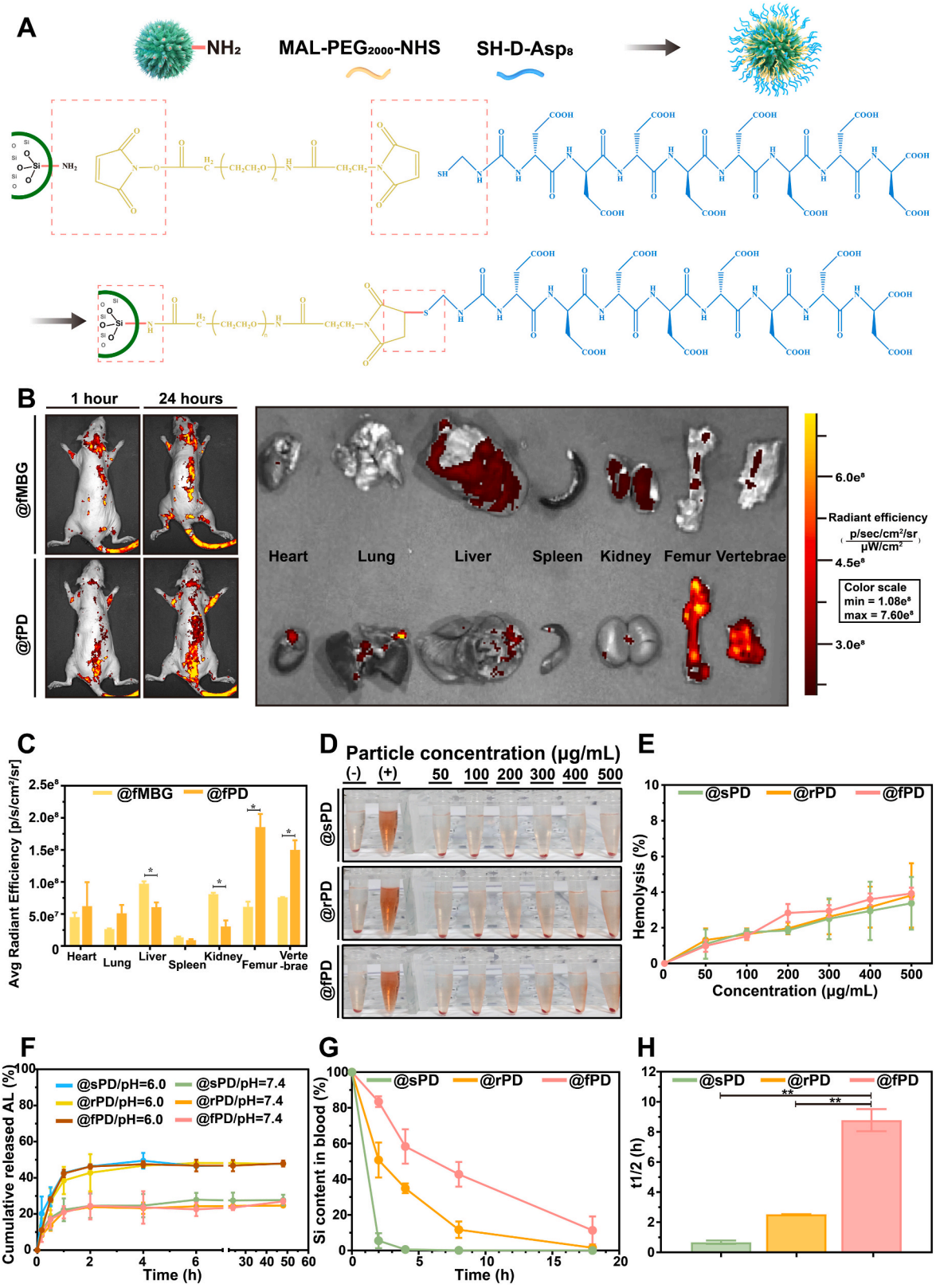

Fig. 2. Bone targeting ability of @fPD and sustained-release performance of AL. (A) Schematic diagram and chemical reaction of functionalized modification of -PEG-DAsp$_8$ represented by aminated fMBG. (B and C) Imaging and quantification of FITC-modified @fMBG and @fPD *in vivo* and organs of rats (n = 3, two-way ANOVA by Sidak's multiple comparison test). Data are presented as the mean ± SEM. (D and E) Hemolysis analysis and quantification of @sPD, @rPD and @fPD at different concentrations of nanoadjuvants (n = 3). (F) AL release curves of @sPD, @rPD and @fPD under pH = 7.4 and pH = 6.0 conditions (n = 3). Data are expressed as mean ± SEM. (G) Changes in blood levels over time after administration of the three systems via the tail vein, calculated as Si content percentage of the injected dose remaining in the blood (n = 3). Data are expressed as the mean ± SEM. (H) Blood circulatory half-life (t1/2) of the three nanoparticles (n = 3). Data are shown as the mean ± SEM. P values < 0.05 are considered statistically significant, and other symbols and their meanings are: *P < 0.05, **P < 0.01.

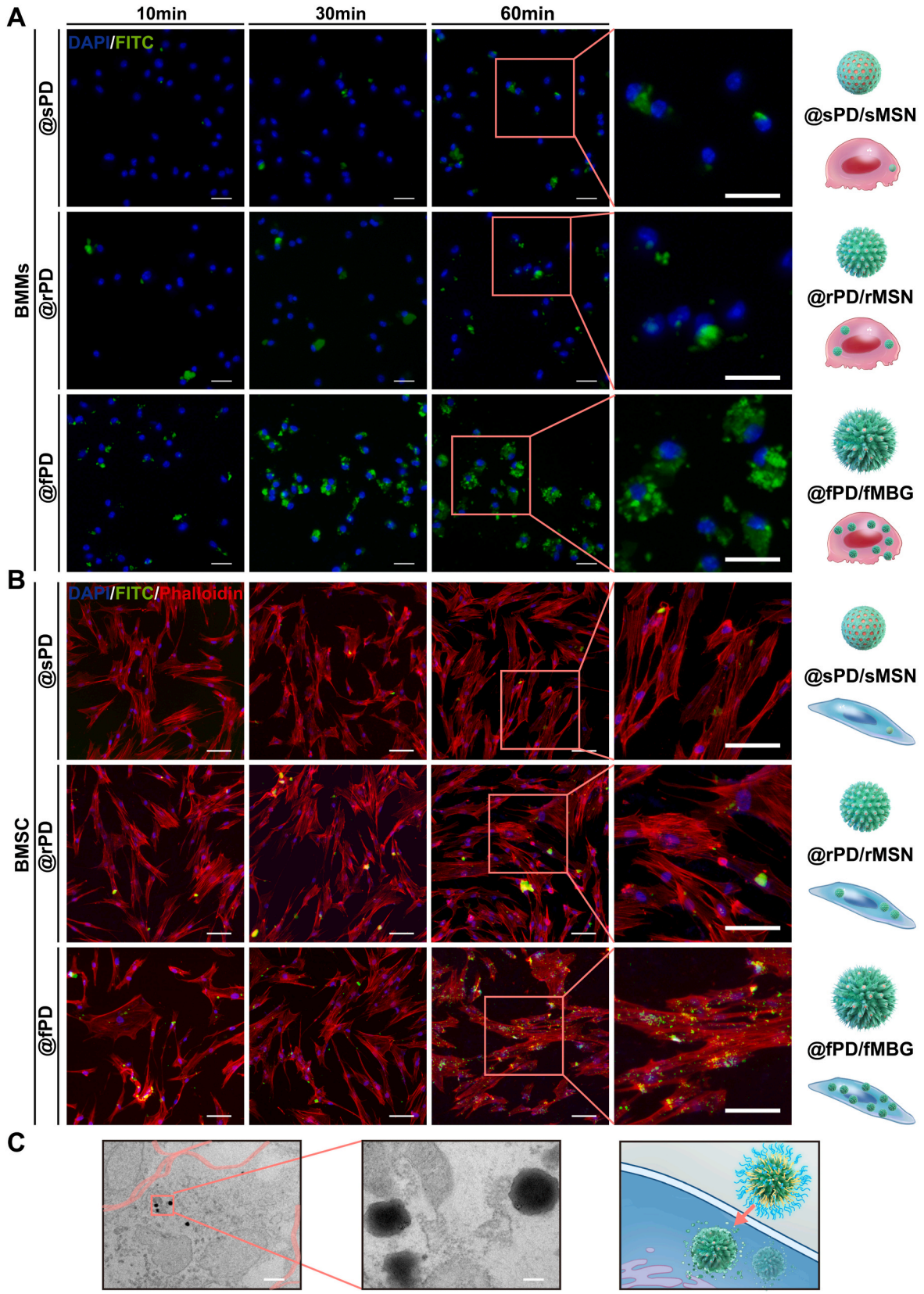

Fig. 3. @fPD has a high cellular uptake rate and intracellular delivery capacity. (A) Representative fluorescence images (scale = 100 μm) and schematic diagram showing the uptake of three FITC-modified nanoadjuvants by BMMs over time. (B) Representative fluorescence images (scale = 100 μm) and schematic diagram illustrating the uptake of three FITC-modified nanoadjuvants by BMSC over time. (C) Transmission electron microscopy (scale = 2 μm) and local magnification (scale = 100 nm) photos and schematic diagram of the co-culture of BMSC with @fPD after 2 h. The cell boundaries are indicated by pink lines.

morphology [33] and eventually obtain the fluffy morphology. Our calcium-phosphate doping fMBG revealed good biological activity *in vitro* [38]. On day 0 and day 1 of simulated body fluid (SBF) soaking, SiO_2 was only detected between 15 and 35°. On day 3 of soaking, Hydroxyapatite (HA) deposition was observed on the surface (Fig. 1H and Supplementary Figure 4A). HA deposition (Fig. 1G) which can be assigned to (211), (310), and (222) reflection peaks [38–40] of bioactive-glass-like fMBG, following Ca–P cross-linking, remains superior to that of sMSN and rMSN owing to more intensive and sharper peaks. This suggests a stronger HA formation capacity, or in other words, enhanced bioactivity, which could be more conducive to promoting the bone formation process *in vivo* [41].

Additionally, maintaining a relatively lower Ca/P ratio can effectively circumvent the issues previously reported, including the release of Ca ions, a decrease in MBG network connectivity, and surface topography damage caused by hydrolysis [42]. As shown in Fig. 1J, our fMBG can retain its surface fluffy morphology under PBS immersion at pH levels of 7.4 or 6.0, respectively. The contents of the P element (Fig. 1I) and Si element (Supplementary Figure 5) in the immersion solution remain relatively stable. The Ca element in the immersion solution, soaked for 1–16 days, consistently remained below the detection line of ICP-AES. This also confirms the structural stability of fMBG, which will be beneficial for long-term maintenance of morphology, drug loading, transportation, and reaction *in vivo*.

3.2. Bone targeting ability of @fPD and sustained-release performance of AL

We introduced MAL-PEG_{2000}-NHS for PEG grafting after the amino functionalization of mesoporous nanoparticles to develop bone-targeting nanoadjuvants with high bioaffinity. This modification improves the bioaffinity of the drug delivery system and reduces its endocytosis by the reticuloendothelial system (RES), which includes organs like the liver and spleen. This, in turn, extends its blood circulation time [18,19,25]. Additionally, asparagine octapeptide with a right-handed structure can rapidly bind to hydroxyapatite, acting as a bone biomimetic peptide. This allows it to specifically target bone tissue [43–46]. SH-D-Asp_8 was used to graft D-Asp_8 to achieve bone targeting of the drug delivery system. Fig. 2A shows the one-pot reaction synthesis technique and its chemical formula. As the intermediate product of fMBG synthesis, sMSN and rMSN were also modified and treated with AL loading to maintain consistency with fMBG. Ultimately, sMSN, rMSN, and fMBG were presented as @sPD, @rPD, and @fPD respectively. The FT-IR in the modification process is shown in Supplementary Fig. 6A-C, with arrows indicating the characteristic peaks of each component. The original SiO_2 characteristic peaks are at 1040 cm^{-1} and 800 cm^{-1}, and the $–NH_2$ characteristic peaks are at 1659 cm^{-1} and 1503 cm^{-1}. The characteristic peaks at 3400 cm^{-1} are attributed to the O–H contraction vibration following targeted modification. The peak at 1660 cm^{-1} corresponds to the stretching vibration of γN-H and the bending vibration of δN-H in the amide [17,18,36]. We also assessed the effects of the entire modification and drug-loading process on the properties of the nanoparticles. Based on TEM images (Supplementary Figures 7-9) and particle size distribution maps (Supplementary Figure 10A), the modification and drug loading did not significantly influence the surface morphology and particle size of the three types of mesoporous nanoparticles. Zeta potential changes are shown in Supplementary Figure 11. To further validate the success of the modification and bone targeting capacity in areas prone to osteoporosis i.e., the femur and vertebrae [6–8], we grafted FITC fluorophores into the nanoadjuvants using FITC non-activator dependent high reactivity to react with exposed $–NH_2$ [33]. The nanoadjuvants size and potential results modified by FITC are presented in Supplementary Fig. 12A-C. As represented by @fPD, the *in vivo* imaging and organ fluorescence results at 1 h and 24 h after injection into the tail vein of rats (Fig. 2B–C) showed that @fPD grafted with -PEG-DAsp_8 significantly improves the targeting capacity of the femur ($p = 0.0301$) and vertebrae ($p = 0.0389$), at the same time relatively reducing the uptake by crucial organs including the liver ($p = 0.0486$) and kidney ($p = 0.0351$). This is unlike the non-modified @fMBG control group. Furthermore, the hemolysis rate of the three nanoadjuvants was less than 5 % (Fig. 2D–E). Therefore, @sPD, @rPD, and @fPD are considered to have successfully undergone targeted bone tissue modification, while ensuring biosafety.

Since the surface grafting modification may affect the pore size, pore volume, and specific surface area, this could in turn influence the drug loading capacity of the drug delivery system [47,48]. The respective pore volumes for sPD, rPD, and fPD were 0.631 cc/g, 0.437 cc/g, and 0.340 cc/g. The BET technique was used to compute the specific surface area of the isotherm, with sPD at 157.308 m^2/g, rPD at 116.931 m^2/g, and fPD at 71.676 m^2/g (Supplementary Figure 13). Consequently, we hypothesized that the drug loading capacity of the three nanoadjuvants would also decrease. Notably, AL is loaded into the nanoadjuvants by simple physical adsorption [49–51] as described above. The AL encapsulation rate/drug loading capacity of the three was quantified using the ninhydrin method [52].

$$EE = \left(\frac{M0 - M1}{M0}\right) \times 100\%$$

(EE is the encapsulation rate; M0 is initial drug quality; M1 is the amount of drug in the supernatant)

The encapsulation rates of @sPD, @rPD, and @fPD were computed respectively (since the initial mass of our nanoparticles is equal to the initial mass of AL, the numerical encapsulation rates in this case are equivalent to the drug loading) (Supplementary Figure 14). The rates, average of 48.3 %, 27.4 %, and 16.8 % respectively, and the successively reduced encapsulation rate/drug loading rates are consistent with our prediction. Considering the *in vivo* action, there may be differences in drug release under various pH conditions [16,33,53]. We also monitored the release process of @sPD, @rPD, and @fPD in a PBS immersion environment with pH values of 7.4 and 6.0, respectively (Fig. 2F). We found that the release process of @sPD, @rPD, and @fPD improved due to the effect of the environmental solution potential [51]. Under acidic conditions, AL is released to a greater extent; however, the release speed significantly slows down with time at both pH levels, reaching a plateau period for almost 48 h in our experiments. Additionally, the drug release process was unaffected by different characteristics of nanoadjuvants; no significant difference was noted in the release modes of @sPD, @rPD, and @fPD. Fig. 2G–H shows the *in vivo* half-life of the three nanoadjuvants, which varies from about 0.5 h for @sPD and about 2 h for @rPD to about 9 h for @fPD. The extended duration of @fPD can ensure a more prolonged *in vivo* action, providing a theoretical basis for stable and long-acting nano-drug delivery treatment. Thus, all our @sPD, @rPD, and @fPD have slow-release properties, with @fPD displaying a longer *in vivo* half-life.

3.3. @fPD has a high cellular uptake rate and intracellular delivery capacity

To study and compare the cellular uptake of different nanoadjuvants with unique topologies, FITC-modified @sPD, @rPD, and @fPD were co-cultured with bone marrow-derived monocytes (BMMs) (Fig. 3A) and bone marrow mesenchymal stem cells (BMSC) (Fig. 3B), respectively. Immunofluorescence composite images and quantitative results of cellular uptake rates (Supplementary Fig. 15A and B) showed that both BMMs and BMSC had a certain level of uptake of the three nanoadjuvants. As the time extended, there was an increase in the uptake of cells in each nanoadjuvants (unit: μg/mg protein). Nevertheless, after 10 min of treatment, @fPD (BMMs: 3.11 ± 0.78; BMSC: 5.80 ± 2.05) demonstrated a higher cellular uptake rate than @sPD (BMMs: 2.61 ± 0.22; BMSC: 2.79 ± 0.53) and @rPD (BMMs: 2.71 ± 1.23; BMSC: 3.55 ± 0.82), and continued to lead @sPD and @rPD for at least further 4 h.

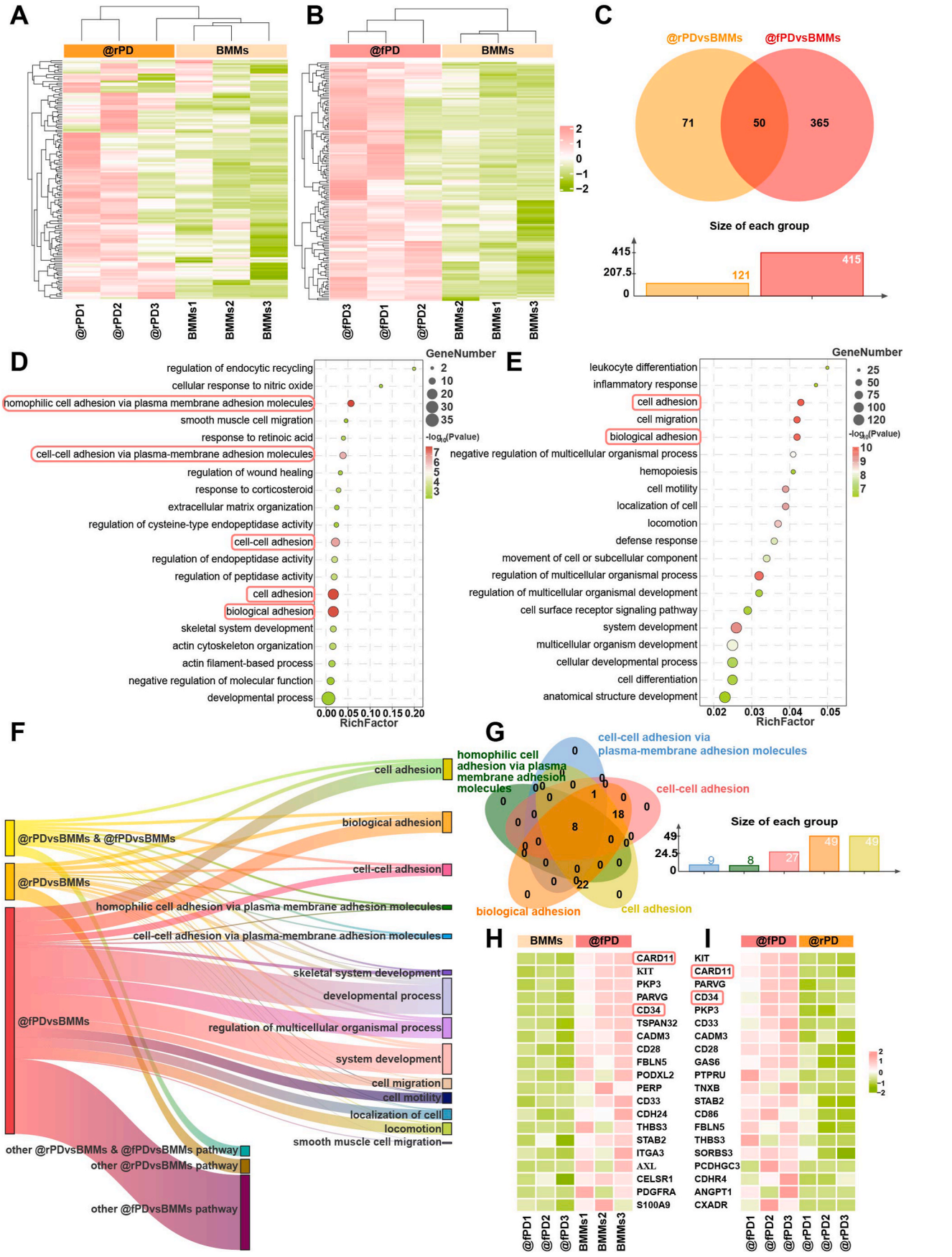

(caption on next page)

Fig. 4. Adhesion pathway activation participants in the differences of cellular uptake rate. (A) Subcluster heat map of differential genes in BMMs group compared with @rPD. (B) Subcluster heat map of differential genes in BMMs group compared with @fPD. (C) Venn diagram of the upregulated differential gene set in @rPD vs BMMs and @fPD vs BMMs. (D) Bubble map of GO pathway enrichment involving upregulated differential genes in @rPD vs BMMs. (E) Bubble map showing the GO pathway enrichment for the upregulated differential genes in @fPD vs BMMs. (F) Sankey analysis diagram of the upregulated differential genes in @rPD vs BMMs, @fPD vs BMMs and their intersection. (G) Combined Venn analysis for @fPD vs BMMs involved in significantly upregulated five adhesion pathways. (H) Sequenced heat maps of the significance of upregulated differential genes in @fPD with BMMs as the control for results shown in (G). (I) Sequencing heat maps of the significance of upregulated differential genes in @fPD with @rPD as control for results in (G).

Considering the 60-min representative BMMs uptake images presented in the paper as an example, compared with @sPD ($p = 0.0077$) and @rPD ($p = 0.0276$), BMMs had a significantly higher uptake rate of @fPD. Finally, at the endpoint of our experiment, i.e., 240min (4h), we can see the results of a similar trend, whether BMMs (@sPD 5.19 ± 0.46, @fPD 11.35 ± 0.94 ($P = 0.0067$)) or BMSC (@sPD 5.04 ± 0.59), @fPD 13.95 ± 0.93 ($P = 0.0148$)), @fPD had obvious advantages in cellular uptake. The uptake of @rPD by cells was consistently and slightly higher than that of @sPD. Summarily, our Ca–P cross-linked fluffy nanoadjuvants, @fPD/fMBG, have a more significant benefit in cellular uptake. Unlike the previous physicochemical characterizations including particle size and Zeta potential and related literature reports [27,28,33], we speculate that the difference in cellular uptake rate is majorly associated with the unique topological morphology of the nanosphere surfaces.

For further insight into the cellular action process of the nanoadjuvants, cells were observed under a transmission electron microscope after their ingestion. As represented by @fPD/fMBG (Fig. 3C), the fluffy surface morphology with a stable structure during the previous days of immersion was interfered with following cellular uptake. The special fluffy surface morphology disappeared, and the mesoporous pore channels became blurred, indicating degradation. A similar phenomenon was also observed in the @sPD and @rPD two groups (Supplementary Figure 17). These structural disruptions and changes are conducive to the complete release of drugs into the cell [48], and the effect of drugs can be significantly exerted.

While studying the cellular uptake rate, CCK-8 experiments were carried out to further validate the biocompatibility of the three nanoadjuvants. After co-culturing the nanoadjuvants at a concentration of 500 μg/mL with BMMs (Supplementary Fig. 17A and B) or BMSC (Supplementary Fig. 18A and B) for different durations and concentrations for 24 h, the cell survival rate for both BMMs and BMSC treated with the three materials consistently exceeded 80 %. No significant difference was observed between the groups. This suggests that our nanoadjuvants have relatively consistent compatibility.

These preliminary results demonstrate that @fPD or fMBG, with their unique fluffy surface morphology, exhibit a stronger cellular uptake capacity. Our nanoadjuvants effectively deliver nano-drugs and release AL into the cells. Additionally, they exhibit good cell biocompatibility. These factors collectively make them promising candidates for further comprehensive research.

3.4. Adhesion pathway activation participants in the differences of cellular uptake rate

After observing the differences in cellular uptake rate caused by nanoadjuvants, we sought to understand the underlying mechanism. Previous studies indicate that a rough surface or spiky structure can decrease the interaction energy between nanoparticles and the cell membrane, which is helpful for endocytosis [28]. However, given that cellular molecules are important drivers of life processes [54], the specific molecular biological mechanisms, particularly the alterations in the cellular signaling pathways, involved in the nanoparticle uptake process warrant further investigation. As such, we used RNA-seq to probe into the possible molecular biological mechanisms underpinning the high cellular uptake rate caused by the Ca–P cross-linked fluffy surface topological morphology of nanoadjuvants.

We performed a comprehensive analysis of the up-regulated gene sets in the @rPD and @fPD treatment groups, using untreated BMMs as controls. The main subcluster heat map (Fig. 4A–B) showed that the part of gene sets was significantly upregulated in both experimental groups treated with @rPD and @fPD systems (Supplementary Figure 23). Moreover, the Venn diagram (Fig. 4C) demonstrated a significant overlap between the upregulated gene sets in the experimental groups, suggesting a common regulatory mechanism during the cellular uptake of different nanoadjuvants. Furthermore, Gene Ontology (GO) analysis was used to assess the pathways involved in the upregulated genes. As illustrated in the bubble diagram (Fig. 4D–E), within different analyses, pathways associated with "adhesion" repeatedly appeared with substantial gene counts and significant differences. These pathways include homophilic cell adhesion via plasma membrane adhesion molecules, cell-cell adhesion via plasma-membrane adhesion molecules, cell-cell adhesion, cell adhesion, and biological adhesion. Although the first three pathways did not rank among the top 20 in the GO analysis for the @fPD treatment group, the Sankey analysis (Fig. 4F) revealed that these five pathways are involved in the upregulation differential clusters. This implies that yet again adhesion pathways i.e., similar regulatory mechanisms, are involved in the uptake of different nanoadjuvants. We firmly propose that the changes in the adhesion pathways represent the common mechanism. Consequently, we compared the BMMs, @rPD, and @fPD sequencing groups on a pairwise basis. To investigate the co-regulatory mechanism of the adhesion pathways, we focused on homophilic cell adhesion via plasma membrane adhesion molecules, cell-cell adhesion via plasma-membrane adhesion molecules, cell-cell adhesion, cell adhesion, and biological adhesion. A Venn analysis was used to artificially enrich the upregulated differential genes involved in all the aforementioned five pathways (Fig. 4G, Supplementary Fig. 24A-E). Subsequently, the consolidated differential genes were sequenced using the Gene Set Enrichment Analysis (GSEA) tool on the online platform, OmicShare Tools, for Gene Ontology (GO) analysis. CARD11, KIT, PKP3, PARVG, and CD34 were the top according to the heat-map arrangement results of the "biological adhesion" pathway-associated differential genes annotated by the platform (Fig. 4H–I). These findings were obtained with the Ca–P cross-linked specific topological morphology of @fPD as the primary subjects of observation.

Intriguingly, previous studies identified CARD11 as a molecular scaffold in a specific region of the plasma membrane. CD34 is a highly glycosylated type I transmembrane protein belonging to the family of sialomucins [55–58]. Considering the interaction between the nanoadjuvants and the cell membrane system during the phagocytosis process, validation experiments specifically targeting CARD11 and CD34 are necessary. As the intermediate filament that links cadherin to the cytoskeleton [59,60], PKP3 also occupies a leading position in the enriched concentration. Relevant wet-lab experiments for its verification (Supplementary Fig. 29) showed no significant difference in each group. Additionally, the proto-oncogene KIT and actin-binding protein PARVG also showed significant performance [61,62]. However, the relevance of these experiments warrants future research.

Summarily, RNA-seq technology was employed to predict the causes behind the variations in the cellular uptake of nanoadjuvants. We ultimately hypothesize that adhesion pathway activation is the key contributing factor to these cellular uptake differences. We selected CARD11 and CD34 representative molecules, implicated in these pathways for subsequent validation experiments.

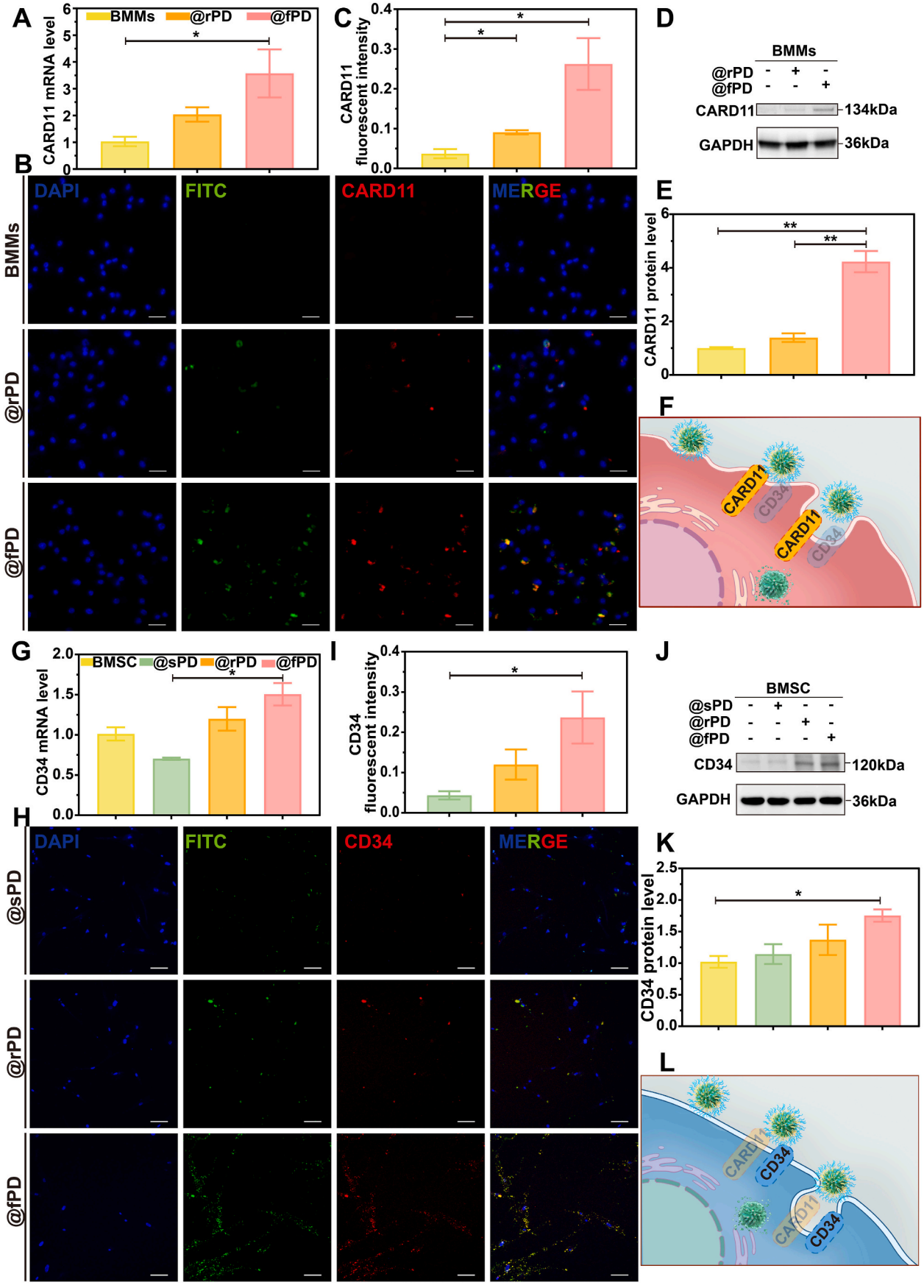

(caption on next page)

Fig. 5. CARD11 and CD34 as the regulatory factors involved in adhesion pathways activation. (A) RT-qPCR analysis of the relative mRNA expression levels of CARD11 in BMMs treated with @rPD or @fPD (n = 5, one-way ANOVA using Tukey ANOVA post hoc test). (B–C) Representative immunofluorescence images of BMMs treated with FITC-modified nanoadjuvants (scale = 25 μm) and quantification. (D–E) Western blot results and the corresponding quantification of CARD11 protein relative expression levels in BMMs treated with @rPD and @fPD (n = 3, one-way ANOVA using Tukey ANOVA post hoc test). (F) The schematic diagram illustrating the endocytosis of @fPD by BMMs. (G) RT-qPCR analysis of the relative mRNA expression levels of CD34 in BMSC treated with @sPD, @rPD and @fPD (n = 5, one-way ANOVA using Tukey ANOVA post hoc test). (H–I) Representative immunofluorescence images of BMSC treated with FITC-modified nanoadjuvants (scale = 100 μm) and quantification. (J–K) Western blot results and the corresponding quantification of relative expression levels of CD34 protein in BMSC treated with @sPD, @rPD and @fPD (n = 3, one-way ANOVA using Tukey ANOVA post hoc test). (L) The schematic diagram illustrating the endocytosis of @fPD by BMSC. Data are presented as the mean ± SEM. P values < 0.05 are considered statistically significant, and other symbols and their meanings are: *P < 0.05, **P < 0.01.

3.5. CARD11 and CD34 as the regulatory factors involved in adhesion pathways activation

To verify our prediction that the differences in uptake observed in RNA-seq are due to the activation of adhesion pathways molecules CARD11 and CD34, RT-qPCR was performed to confirm CARD11 and CD34 expression at the RNA level, both in BMMs and BMSC of their @rPD and @fPD treatment groups (Fig. 5A and Supplementary Fig. 27). As expected, the @fPD-treated group consistently had high expression intensity. The mRNA expression level of CARD11 in the @fPD treated group was significantly higher than that in the control group (P = 0.0392 for BMMs, P = 0.0009 for BMSC). Similar results were also obtained in CD34 mRNA expression (P = 0.0045 for BMMs, P = 0.0157 for BMSC). Further, Western blot experiments demonstrated that the intensity of CARD11 expression was significantly higher than that of BMMs and @rPD treated group (P = 0.0056). While in the series of validation experiments at BMSC, the protein level presented an inconsistent result with BMMs. Specifically, CD34 expression in the @fPD treated group was higher than that in the BMSC control group (P = 0.0458) in Western blot assays (Fig. 5J–K). Regarding the above results, CARD11 and CD34 are significantly up-regulated when treated with nano-adjuvant. However, in the process of specific translation into protein, different specific major carriers exist in different cells which might be attributable to post-transcriptional regulation [63]. CARD11 plays a major adhesion and uptake-related processes in the BMMs-related treatment group, whereas in BMSC, this role is largely assumed by CD34.

To further verify the involvement and instant expression of CARD11 and CD34 in BMMs and BMSC during the uptake of nanoadjuvants, we directly co-cultured different FITC-modified systems with BMMs (Fig. 5B–C) and BMSC (Fig. 5H–I) for 1 h each before performing immunofluorescence experiments. In line with previous experimental results, FITC-labeled @fPD consistently had the highest cellular absorption rate. Simultaneously, the signal intensity of CARD11 in BMMs was highly consistent with the merged signal of ingested FITC-labeled nanoadjuvants. In BMSC however, the signal intensity of CD34 strongly corresponded with the FITC signal of the systems. Moreover, we also observed the highest uptake of @fPD and the highest signal intensity of protein molecules, with the location and intensity of the two showing significant correlation. These results further confirm that @fPD can more effectively activate the CARD11-involved adhesion pathways in BMMs for high cellular uptake, whereas the high uptake of @fPD in BMSC and the differences in uptake of other nanoadjuvants are associated with CD34 activation.

In summary, we verified the RNA-seq prediction results in BMMs and BMSC, respectively. The validation outcomes demonstrated that CARD11 and CD34 are the regulatory factors involved in adhesion pathway activation and the uptake differences of nanoadjuvants, particularly mediating the high uptake of @fPD.

3.6. @fPD effectively inhibited osteoclasts and potentially promoted osteogenesis

To ascertain the actual inhibitory effect of the three AL nanoadjuvants on the osteoclast process, we intervened with BMMs during the osteoclasts (OCs) formation. Based on R.A.B. Silva and S. Hu et al. [64,65], we established the concentration gradients of the three systems at 10, 30, 50, and 100 μg/mL (Supplementary Fig. 30) for experiments. Based on the TRAP staining results of treated osteoclasts, a concentration of 50 μg/Ml was selected to investigate the inhibitory effect on osteoclasts by co-culturing. This concentration was selected as the positive rate of TRAP staining significantly decreased in the @fPD group at 50 μg/mL, despite the @sPD and @rPD treatment groups at the same or higher concentration (100 μg/mL) not showing a significant decrease in the positive rate of TRAP. Thus, we performed TRAP staining with quantification (Fig. 6A–C), and TRITC Phalloidin fluorescence staining with quantification (Fig. 6D–E and Supplementary Fig. 31-A) on the OCs after co-culturing with three nanoadjuvants at 50 μg/mL concentration. The results revealed that although the drug loading rate of @fPD was 16.8 % at a similar concentration, lower than that of @sPD (48.3 %) and @rPD system (27.4 %), @fPD still had a stronger inhibitory capacity on osteoclast formation. Unlike the OCs control group, @fPD significantly reduced the number of osteoclasts, the proportion of osteoclasts, and the area of F-actin rings; the effect was superior to that of the @sPD and @rPD treatment groups. In addition to the above morphological detection, we implanted BMMs treated with AL nanoadjuvants onto bone slices and continued osteoclast differentiation induction to further confirm the highly effective osteoclast inhibition effect of @fPD, particularly the functional status of osteoclasts. After 7 days, SEM imaging was performed to observe the situation of bone resorption lacunas (Fig. 6F) and quantification (Fig. 6G and Supplementary Fig. 31-B). Consequently, unlike the OCs control group, the @fPD system outperforms @sPD and @rPD in inhibiting the bone resorption capacity of osteoclasts, as shown by the percentage of bone resorption lacunas and the number of lacunas. Since TRAP, C-FOS, CTSK and DC-STAMP are osteoclast-related markers [66–69], which can be used to test the osteoclast activity, RT-qPCR results (Fig. 6H–I and Supplementary Fig. 31C and D) demonstrated that @fPD could still more effectively down-regulated the expression of these markers despite the expression of osteoclast markers in the induce BMMs not being reduced to the same level as in the negative control group. This further confirms that @fPD is superior to @sPD and @rPD in suppressing the osteoclast activity.

These findings indicate that, despite a lower drug loading rate owing to an increase in particle size and decrease in specific surface area as well as pore volume during @fPD synthesis, the fluffy bioactive glass nanoadjuvants formed by Ca–P cross-linking have a higher cellular uptake and intracellular delivery features, presenting a more efficient treatment effect. This also clarifies why only the @fPD treatment group exerts a substantial decrease in the TRAP staining positive rate at a lower concentration (50 μg/mL).

Considering the unbalanced bone niches of over-activated osteoclasts, inadequate osteogenesis in osteoporosis, and reports from other studies indicating that high AL concentration inhibits osteogenesis [70,71], osteogenic differentiation was induced using BMSC with osteogenic differentiation potential while adding @sPD, @rPD, and @fPD at similar concentrations (also 50 μg/mL as mentioned before). The ALP staining results on the 14th day of induction (Fig. 6J) and ARS staining results on the 21st day (Fig. 6K) were observed macroscopically and microscopically, respectively. The absorbance of ARS was quantified (Fig. 6N), showing no significant difference among all groups. Since OPN and ALP can be used as RNA markers of osteogenesis to evaluate osteogenic activity, RT-PCT was used to detect mRNA expression levels of OPN and

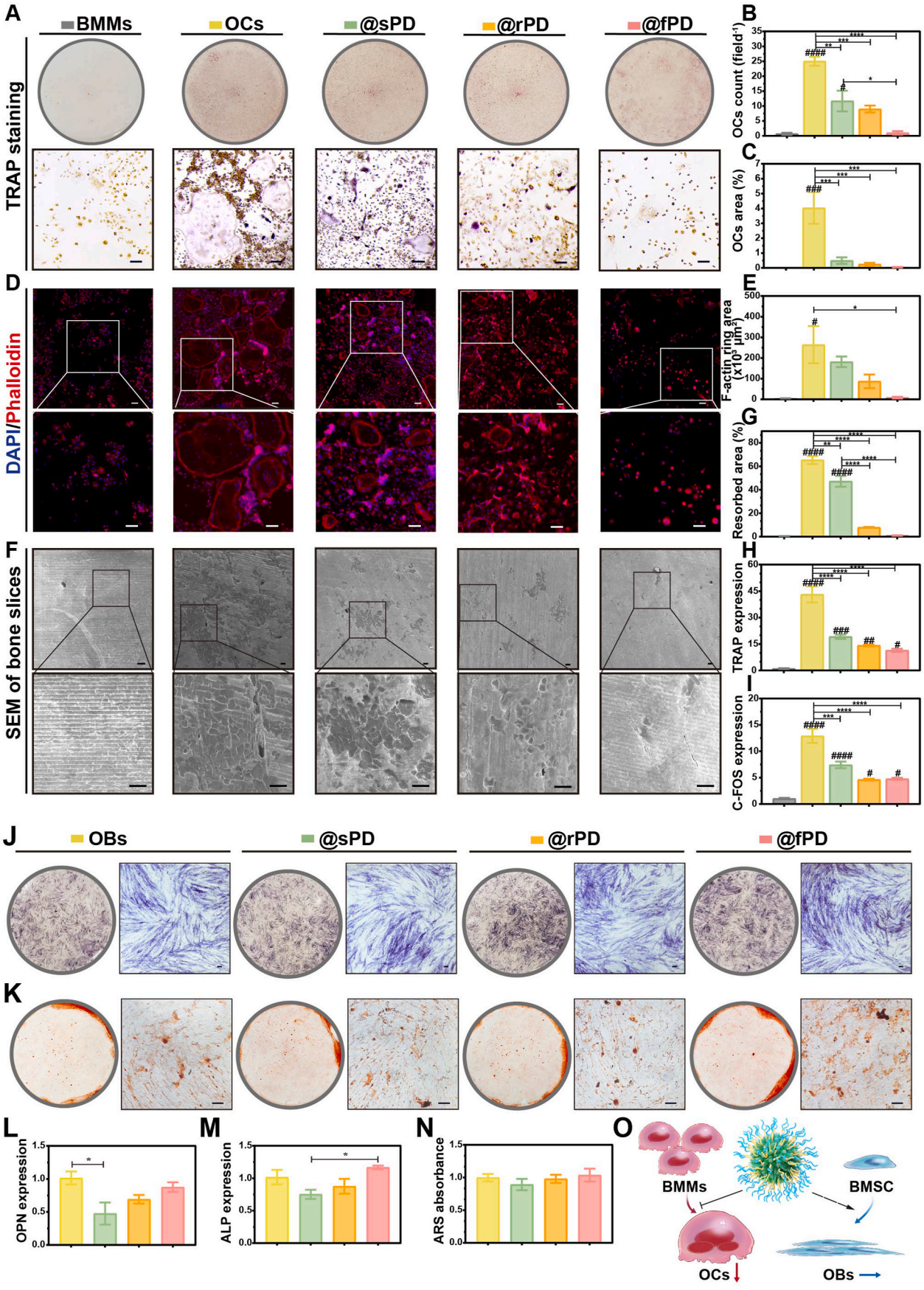

(caption on next page)

Fig. 6. @fPD effectively inhibited osteoclasts and potentially promoted osteogenesis. (A) Representative macroscopic and microscopic TRAP staining images of @sPD, @rPD, @fPD co-cultured with osteoclasts (scale = 100 μm), and their corresponding quantification (B–C) (n = 3, one-way ANOVA using Tukey ANOVA post hoc test). (D) TRITC Phalloidin fluorescence staining and enlarged images of @sPD, @rPD, and @fPD co-cultured with osteoclasts (scale = 100 μm), and their corresponding quantification (E) (n = 3, one-way ANOVA using Tukey ANOVA post hoc test). (F) A representative bone slice absorption SEM image and enlarged images (scale = 50 μm), and the corresponding quantification analysis (G) (n = 3, one-way ANOVA using Tukey ANOVA post hoc test). (H–I) Comparison of mRNA expression levels associated with osteoclast in each group (n = 5, one-way ANOVA using Tukey ANOVA post hoc test). (J) Representative ALP staining (scale = 100 μm) and (K) ARS staining macroscopical and microscopical images (scale = 100 μm) of BMSC treated with @sPD, @rPD and @fPD after osteogenic induction. (L–M) The mRNA expression levels of osteoblast-related genes after osteogenic induction of BMSC (n = 5, one-way ANOVA using Tukey ANOVA post hoc test). (N) Absorbance quantification of the staining results of ARS represented by (K) (n = 3, one-way ANOVA using Tukey ANOVA post hoc test). (O) The schematic diagram illustrating the mechanism of @fPD-induced inhibition of osteoclasts while maintaining osteogenesis. Data are expressed as mean ± SEM. P values < 0.05 are considered statistically significant, and other symbols and their meanings are: *P < 0.05, **P < 0.01, ***P < 0.001, ****P < 0.0001; #P < 0.05, # #P < 0.01, # # #P < 0.001, # # # #P < 0.0001, vs. Control group (default is group 1 in the corresponding experiment).

ALP (Fig. 6L-M). Although there was no statistically significant difference between the @rPD and @fPD treatment groups compared to the normally-induced positive osteoblast OBs, we found that the expression level of ALP in the @fPD treatment group was significantly higher than that of @sPD (P = 0.0173). Additionally, all osteogenic indicators in the @sPD treatment group were lower than the normal level, among which OPN expression was significantly lower than that in the normal induction OBs group (P = 0.0160), suggesting the possibility of osteogenic inhibition. Previous investigations have shown that the Si element is conducive to osteogenesis [72,73]; although @sPD contains the Si element, our findings are inconsistent with this. We believe this may be attributed to osteoblast activity inhibition due to the high AL drug load of @sPD in the culture system [70,71].

Therefore, @fPD can more effectively suppress osteoclasts, even at low AL loading levels. Simultaneously, due to its Ca–P cross-linked fluffy topological morphology, small-dose AL delivery capacity and the characteristics of bioactivity, @fPD exhibits certain bone-promoting potential without interfering with the osteogenesis process of BMSC.

3.7. @fPD reverses osteoclastic-osteogenic imbalance in ovariectomized rats

To confirm the treatment efficacy of @fPD *in vivo*, we used the broadly accepted ovariectomized rat model, which is a standard model for studying osteoporosis. This model mimics postmenopausal osteoporosis, allowing us to investigate the effect of @fPD on bone formation and remodeling under estrogen deficiency-induced bone loss [74–76]. After three months of inducing osteoporosis through ovariectomy, tail vein therapy was administered biweekly. Before the onset of treatment, the successful establishment of the osteoporotic model and the efficacy of AL therapy were confirmed via imaging and histological analysis (Supplementary Figure 33-34). In brief, unlike the sham surgery group, the ovariectomized (OVX) group demonstrated substantial bone lesions in terms of cancellous bone mass (BV/TV), trabecular number (Tb.N), and trabecular separation (Tb.Sp) after three months of regular feeding. After the standard dose AL treatment, the above indicators can return to the sham surgery group. The above results confirm the successful induction of osteoporosis and the efficacy of AL therapy, setting the stage for subsequent nanoadjuvants therapeutic interventions presented in the Supplementary Information.

After confirming the success of the osteoporosis model, we validated the tail vein injection therapy in ovariectomized rats. The control group was the OVX group treated with PBS, whereas the intervention groups were treated with three nanoadjuvants: @sPD, @rPD, and @fPD. To further study the contribution of bone targeting to the therapy, we incorporated the @fMBG group, which carried AL without modification for bone-targeting biological activity. The TRAP staining results (Fig. 7B–F) revealed that the @fPD group significantly reduced the relative perimeter of osteoclasts (OC.N/BS in mm^{-1}) and the area ratio of osteoclasts (OC.S/BS in %). For instance, taking OC.S/BS in femur TRAP staining as an example (Fig. 7C–D), the OVX control group was 56.655 ± 6.045. The @sPD was 35.995 ± 3.485 (p = 0.0442), the @rPD was 28.865 ± 2.835 (p = 0.0133), the @fMBG was 20.500 ± 1.700 (p = 0.0042), and the @fPD was 13.575 ± 1.575 (p = 0.0019). Among them, the @fMBG treatment group had a good inhibitory effect on osteoclasts; however, due to the lack of bone targeting, its capacity to suppress osteoclasts was still inferior to that of @fPD. Thus, @fPD exerted the best osteoclast inhibition effect, consistent with *in vitro* cell experiments. This was attributed to the Ca–P cross-linked fluffy topological morphology of @fPD, its superior cellular uptake and intracellular AL delivery capacity, effective bone targeting, and longer *in vivo* half-life unlike @sPD and @rPD.

To further validate the effect of the nanoadjuvants on the osteogenic activity in osteoporotic rats, we performed OCN immunohistochemical staining (Fig. 7G) as well as quantification on the femur (Fig. 7H) and the vertebrae (Fig. 7I) of rats in each group. Consequently, we found no statistically significant difference in the relative positivity of OCN across all groups. This suggests that each drug delivery system did not influence the osteogenic activity in osteoporotic rats during the experimental observation period. Combined with clinical practice, the osteogenic inhibition in the @sPD group with high AL drug loading might take a longer time to become observable, while the osteogenic potential of the @fPD treatment group remains the same. This further supports the candidature of @fPD as a promising therapeutic agent due to its balanced role in both osteoclast inhibition and osteogenic activity.

Therefore, the *in vivo* experiments regarding osteoclast activity and osteogenesis have yielded results consistent with the *in vitro* cell experiments. @fPD can more effectively inhibit osteoclasts in the tissues of ovariectomized osteoporotic rats due to its Ca–P cross-linked fluffy topological morphology, high cellular uptake rate, bone targeting, and extended half-life. Importantly, it accomplishes this without disrupting the overall level of osteogenesis, hence achieving an efficient AL treatment effect at a small dose. This demonstrates the potential of @fPD as a therapeutic approach for managing osteoclastic-osteogenic balance in osteoporosis.

3.8. @fPD restores the bone niches and bone mass

After evaluating the effects of various nanoadjuvants on osteoclastic and osteogenic activities, @fPD exhibited the most effective osteoclast inhibition without interfering with osteogenesis. Previous studies indicate that postmenopausal osteoporosis causes bone mass loss due to the imbalance between overactive bone resorption mediated by osteoclasts and insufficient bone formation. Therefore, to further assess the overall effect of each nanoadjuvant on a bone mass following treatment of ovariectomized osteoporotic rats, micro-computed tomography (micro-CT) was used to measure the bone mass of femur and vertebrae in ovariectomized osteoporotic rats. Additionally, Hematoxylin and Eosin (H&E) staining was employed to further observe and quantify bone mass at the histological level. This combination of imaging and histological techniques provides a comprehensive understanding of the efficacy of these nanoadjuvants in mitigating bone mass loss associated with osteoporosis.

The micro-CT results of the femur (Fig. 8A) and vertebrae (Fig. 8F) revealed that the bone volume fraction (BV/TV) of cancellous bone in the OVX group was 2.332 ± 1.024 in the femur and 15.092 ± 0.869 in

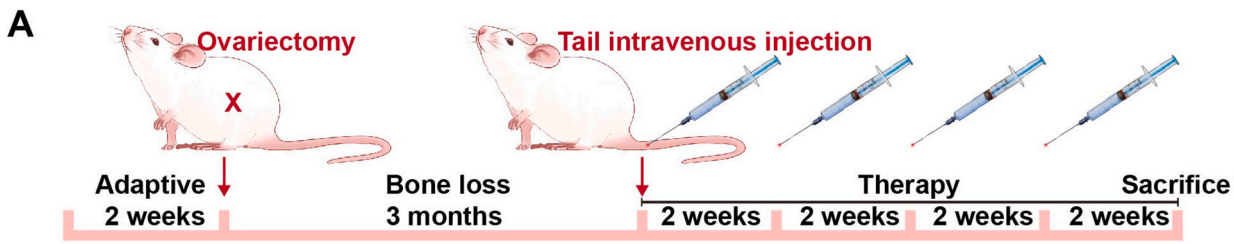

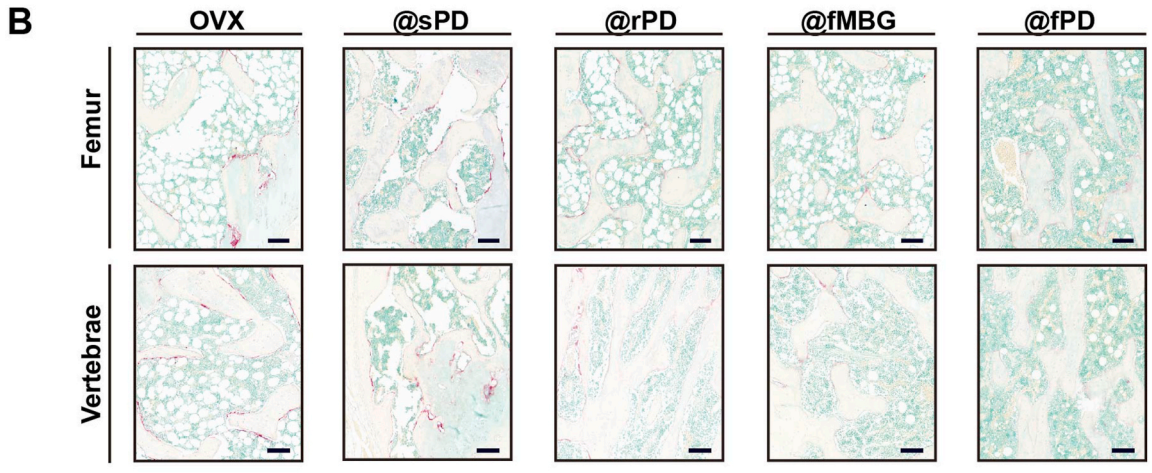

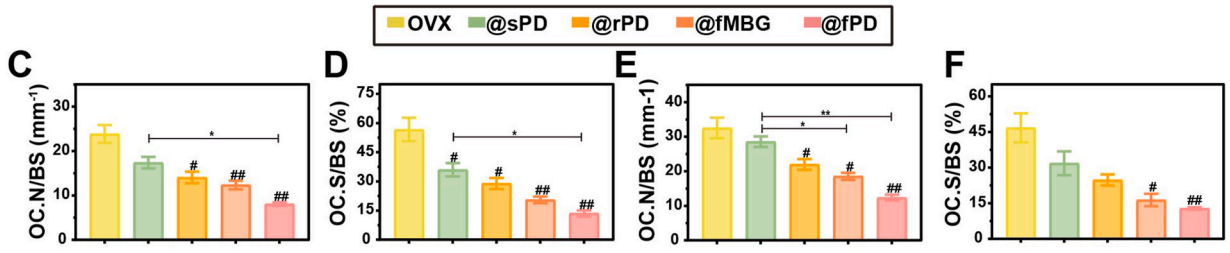

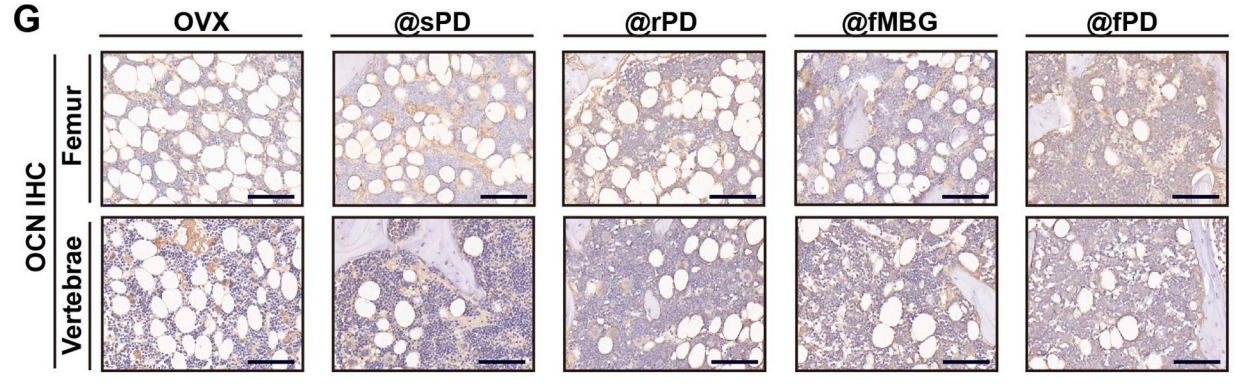

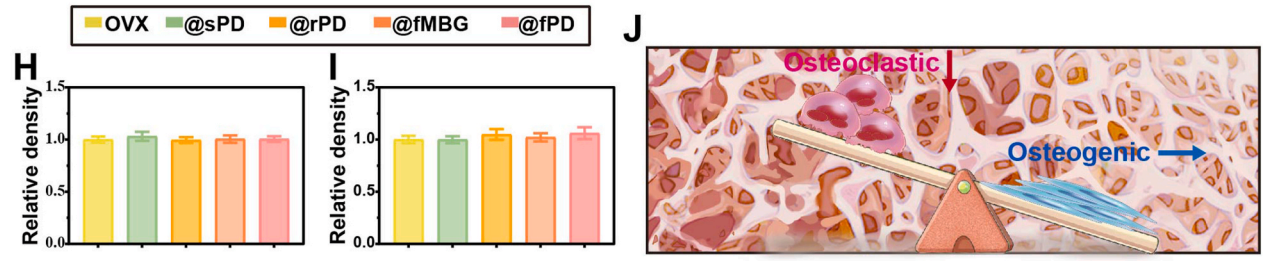

(caption on next page)

Fig. 7. @fPD reverses osteoclastic-osteogenic imbalance in ovariectomized rats. (A) Schematic diagram showing the construction and treatment process of the ovariectomized osteoporosis rat model. (B) Representative femur and vertebrae images in the TRAP staining assay (scale = 100 μm). (C–D) Quantification of the results of TRAP staining of the femur (n = 4, one-way ANOVA using Tukey ANOVA post hoc test). (E–F) Quantification of TRAP staining results for vertebrae (n = 4, one-way ANOVA using Tukey ANOVA post hoc test). (G) Representative images (scale = 100 μm) of immunohistochemical staining of OCN in femur and vertebrae samples of ovariectomized rats with osteoporosis. (H) The degree of OCN positive staining in femur in (G) (n = 4, one-way ANOVA using Tukey ANOVA post hoc test). (I) Quantification of degree of OCN positive staining in vertebrae in (G) (n = 4, one-way ANOVA using Tukey ANOVA post hoc test). (J) Schematic diagram of osteoclastic-osteogenic balance and bone mass recovery in osteoporosis. Data are presented as the mean ± SEM. P values < 0.05 are considered statistically significant, and other symbols and their meanings are: *P < 0.05, **P < 0.01, ***P < 0.001, ****P < 0.0001; #P < 0.05, # #P < 0.01, # # #P < 0.001, # # # #P < 0.0001, vs. Control group (default is group 1 in the corresponding experiment).

the vertebrae. The trabecular number (Tb.N) was 0.252 ± 0.112 in the femur and 1.245 ± 0.097 in the vertebrae. The trabecular separation (Tb.Sp) was 1.517 ± 0.042 in the femur and 1.221 ± 0.134 in the vertebrae. In contrast, @fPD consistently held a dominant position in therapy. It significantly improved the BV/TV of ovariectomized osteoporotic rats (15.314 ± 0.678 in the femur; 20.860 ± 1.215 in the vertebrae), the Tb.N (1.730 ± 0.077 in the femur; 1.759 ± 0.182 in the vertebrae), and the Tb.Sp (0.351 ± 0.014 in the femur; 0.650 ± 0.160 in the vertebrae). This was superior to other treatment groups, reaffirming the importance of efficient nanodrug delivery and bone tissue targeting. Interestingly, in multiple datasets, the therapeutic effect of @fMBG was superior to that of @sPD, demonstrating a therapeutic effect similar to the @rPD group. Although the trabecular thickness (Tb.Th) did not show significant changes in either the normal group, the pine bone group (Supplemental Fig. 33E and I), or during treatment (Supplemental Fig. 35A and B), similarly, no significant differences were observed in cortical bone (Supplemental Fig. 36A and B). This could be related to the osteoporosis development stage in this work. Previous studies have shown that it takes a longer time for the pathological process of osteoporosis to produce differences in these two indexes [77]. Therefore, the above results underscore the significance of our bone-targeting fluffy bioactive glass nanoadjuvants.

Histologically, H&E staining and quantitative analysis were conducted on the distal femur and the vertebrae, respectively (Fig. 8E and J). The results were consistent with the micro-CT findings, indicating that @fPD had the most beneficial impact on improving bone mass in ovariectomized osteoporotic rats (femur 72.285 ± 3.470, $p < 0.0001$; vertebrae 78.600 ± 2.509, $p < 0.0001$). This further underscores the therapeutic potential of @fPD in treating osteoporosis. The quantitative histological analysis aligns with the imaging results, suggesting a robust improvement of bone mass after treatment with @fPD, thereby providing a promising strategy for osteoporosis management.

The carboxy-terminal cross-linked telopeptide of type 1 collagen (CTX-1) and procollagen type 1 N-terminal propeptide (PINP) are serological markers of osteoclastic and osteogenic activities, respectively [53]. We also measured the levels of CTX-1 and PINP in osteoporotic rats and treatment groups (Supplementary Figure 37). Although the results varied among different groups, the CTX-1 and PINP levels in the nanoadjuvants treatment groups tended towards those of the normal control group. This suggests that the treatments are effective in restoring the balance between bone resorption and formation, which is disrupted in osteoporosis. The larger differences observed in the results could be attributed to changes in the dynamic balance of osteoclasts and osteogenesis during bone mass regulation. This informs the complexity of bone remodeling and the need for meticulous monitoring of these markers during treatment.

In conclusion, our experimental results indicate that @fPD efficiently restores the imbalanced niches of osteoclastic-osteogenic in osteoporosis, resulting in bone mass recovery.

4. Discussion

To improve efficacy while minimizing drug side effects in the treatment of osteoporosis, we developed fluffy hybrid nanoadjuvants for enhancing the bioavailability of Alendronate (AL) as a treatment of osteoporosis. The use of nanoadjuvants improved the efficient intracellular delivery of AL at low doses while maintaining biocompatibility, bone targeting, and prolonged half-life *in vivo*. Moreover, the molecular mechanisms, particularly those of cellular uptake during therapy. The application of the nano-adjuvant optimized the therapeutic efficacy of AL by ameliorating the imbalance in osteoclastic-osteogenic niches in osteoporosis and preserving bone mass in ovariectomized rats.

The capacity of the @fPD to load small-dose AL may be due to its reduced specific surface area and pore volume during preparation. Based on this property, the synthesized materials exhibited distinct morphologies and fluffy surface topology. This was achieved through the oil-water biaxial epitaxial method and the introduction of calcium and phosphorus elements [33,37]. Initially, the results exhibited outward growth with a rough morphology on silica nanosphere surfaces when TEOS was used as a raw material. Subsequently, it transitioned to a Ca–P cross-linked fluffy morphology after doping with $Ca(NO_3)_2{\cdot}4H_2O$ (CNT) and triethyl phosphate (TEP) to modify the original Si–O structure and achieve a rough morphology to Si, O, Ca, and P cross-link fluffy topological structure. Traditional bioactive glass often has a high calcium-phosphorus ratio, which can destabilize nanoparticles and change their surface structure [36,38,42]. In contrast, our nanoadjuvants, made from a bioactive-glass-like material, offer several advantages. First, their lower calcium and phosphorus content creates a unique, fluffy surface morphology. Second, they remain stable in solution despite this difference in composition. Importantly, they retain their strong biological activity and ability to promote hydroxyapatite deposition.

Although this unique topological morphology decreases the drug load capacity, it is a valuable factor when considering AL as the standard treatment for osteoporosis. AL is linked to the occurrence of numerous dose-related adverse reactions, that limit its clinical benefits [4,5,14,15,70,71]. The results demonstrated that the utilization of @sPD with a high AL loading rate partially suppressed osteogenic differentiation of bone marrow stromal cells (BMSC) to some extent, whereas administration of small doses of AL by @fPD did not compromise the osteogenic activity of BMSC. Furthermore, the dynamic interplay between calcium and phosphorus in our material (@fPD) contributes to its bone-building potential by mimicking the natural osteogenic bioactivity. These findings suggest that @fPD could serve as a safer and more effective alternative to osteoporosis treatment by reducing the harmful effects associated with high doses of AL.

Despite exhibiting a lower drug loading capacity compared with the pre-reaction products @sPD and @rPD, @fPD demonstrates superior therapeutic efficacy in AL delivery. Specifically, it prevents the formation and functionality of osteoclasts, thereby mitigating bone loss in rats with osteoporosis. The enhanced efficacy of low-dose therapy could be due to the fluffy topological morphology of Ca–P crosslinks, which promotes intracellular delivery of AL. Although they have larger particle sizes relative to the intermediates sMSN and rMSN, the modified fMBG and @fPD have high rates of cellular uptake. Notably, within 10 min after treatment, fluffy @fPD showed increased cellular uptake compared to @sPD and @rPD, which persisted for at least 4 h post-treatment. This finding matches that reported in previous studies suggesting that the rough morphology of nanoparticles improved the cellular uptake [27,33,78]. In this study, we found that even though the rough surface morphology of the material reduces its specific surface area and pore volume, leading to a lower drug load, its effectiveness in delivering

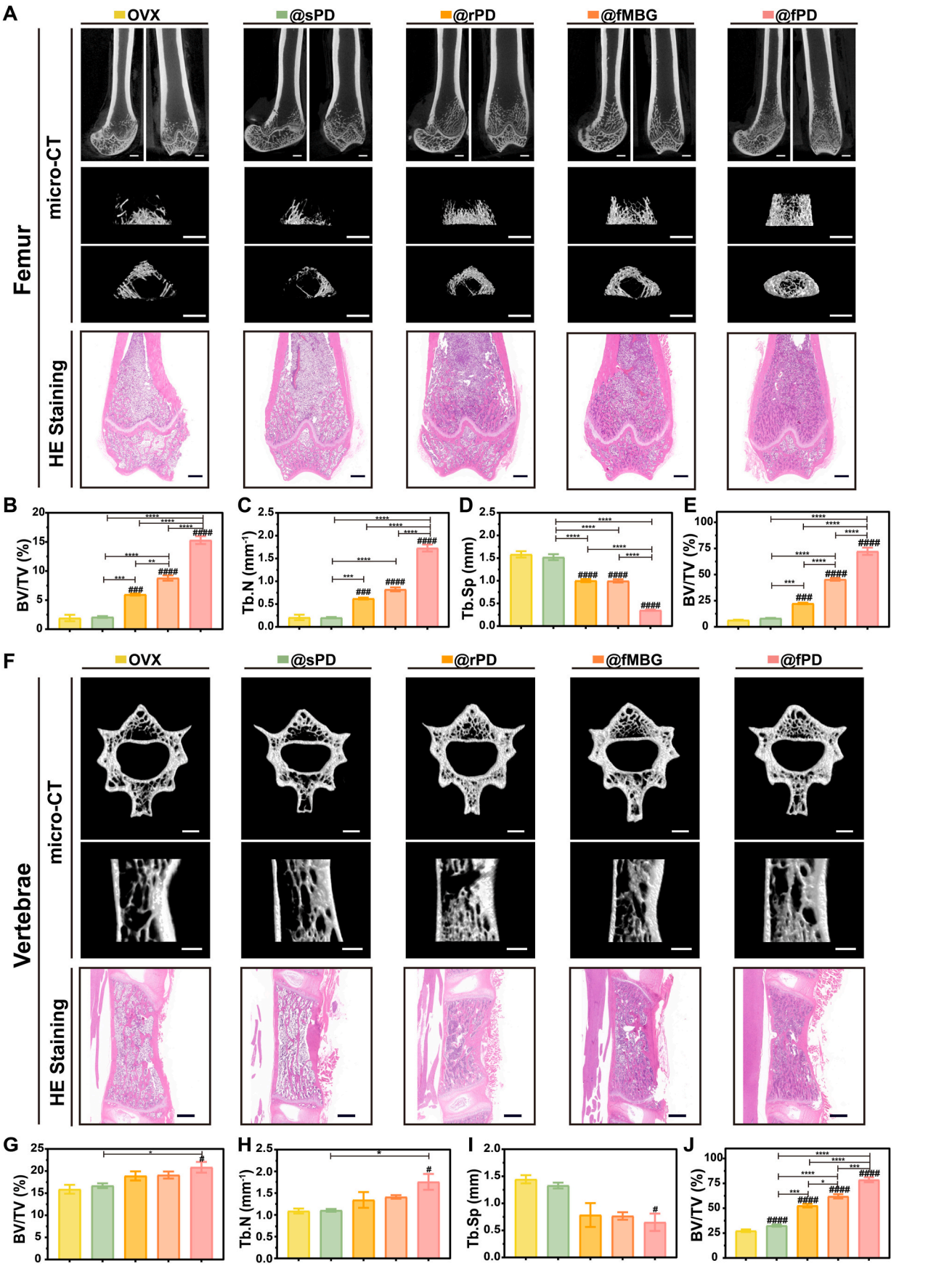

(caption on next page)

Fig. 8. @fPD restores the bone niches and bone mass. (A) Representative micro-CT and HE staining images of femur (scale = 1 mm). (B–D) Quantitative analysis of micro-CT results of femur (n = 4, one-way ANOVA using Tukey ANOVA post hoc test). (E) Quantitative analysis of HE staining results of the femur (n = 4, one-way ANOVA using Tukey ANOVA post hoc test). (F) Representative micro-CT images and HE staining of vertebrae (scale = 1 mm). (G–I) Quantitative analysis on the micro-CT results of vertebrae (n = 4, one-way ANOVA using Tukey ANOVA post hoc test). (J) Quantitative analysis of HE staining images of vertebrae (n = 4, one-way ANOVA using Tukey ANOVA post hoc test). The data are expressed as the mean ± SEM. P values < 0.05 are considered statistically significant, and other symbols and their meanings are: *P < 0.05, **P < 0.01, ***P < 0.001, ****P < 0.0001; #P < 0.05, # #P < 0.01, # # #P < 0.001, # # # #P < 0.0001, vs. Control group (default is group 1 in the corresponding experiment).

drugs intracellularly is significantly improved. This enhanced intracellular delivery compensates for the reduced drug load and ultimately leads to a stronger therapeutic effect. These findings align with observations made in oncology studies [33]. Notably, as anticipated, our nanoadjuvants significantly enhanced bone targeting ability and prolonged *in vivo* half-life following the modification grafting [18,19,25]. These manipulations augmented the therapeutic effect of the drug regardless of the dose and enhanced the therapeutic efficiency of lower drug doses. Based on these, we infer that nanoadjuvants can decrease the incidence of adverse reactions caused by excessive doses or long-term drug accumulation following low-dose administration in clinical settings.

Majority of previous have mainly investigated the physical models, energy relationships, and lysosome-related clearance processes to explore interactions between nanoadjuvants and cells [27,28,79]. However, few studies have elucidated the impact of changes in relevant signaling pathways on the overall uptake process and the molecular contributions of different uptakes induced by different topological morphologies. In this study, high-throughput RNA-seq technology and customized innovative protocols were employed to facilitate the screening of differentially expressed genes (DEGs) thus predict potential protein molecules. To confirm the sequencing and prediction results, we performed experiments like RT-qPCR, Western blotting, and immunocytochemistry (ICC/IF). These experiments revealed that the adhesion gene ontology (GO) pathway plays a crucial role in how cells take up nanoadjuvants with different surface shapes (morphologies). This process appears to be mediated by two specific membrane proteins: CD34 and CARD11. This finding expands our understanding of the cellular uptake processes of nanoadjuvants from a molecular biological perspective and provides valuable insights to guide future therapeutic strategies based on the design of small molecule structures targeting CARD11 or CD34. Our results indicate that drug intracellular delivery is not only influenced by the design of the surface structure of nanoparticles, but also possibly by its molecular mechanisms.

However, our study also has some limitations. *In vivo*, we controlled for consistent doses of different nanoadjuvants, and found that AL low-load @fPD treatment group had better performance compared with multiple nanoadjuvant groups in a rat ovariectogenous osteoporosis model. We stained tissue sections using a technique called TRAP staining and performed histological analysis related to osteoclastic-osteogenesis. This analysis revealed that @fPD effectively inhibited bone resorption by osteoclasts. This inhibition likely results from the material's efficient delivery of a molecule called AL. By regulating osteoclast activity, @fPD helps restore a healthy balance in the bone microenvironment and prevents bone loss. These findings are consistent with the results we observed in our cell-based experiments *in vitro*. The Ca–P cross-linked fluffy structure improved the drug delivery. However, we provided the bone mass related section photos and data of the AL standard treatment group in the supplementary materials. While the bone mass in the @fPD group did not fully recover to the same level as the standard AL treatment group, there was a clear and consistent trend of improvement compared to the sham surgery group. This positive trend supports our overall conclusion about the effectiveness of the @fPD treatment. Concerning the inadequate therapeutic effect associated with multiple nanoadjuvant groups, we postulate that the most important reason may be the actual amount of AL utilized. Unlike previous studies where we compared the overall effect of different nanoadjuvant amounts, this study examined nanoadjuvants with varying capacities to load and release AL. This approach differs from the standard AL treatment group, where the drug delivery method is different. In this case, analysis of multiple nanoadjuvant systems revealed that @fPD promoted the therapeutic effect of low-dose AL, which cannot be explained solely from the perspective of AL. Generally, many drugs, including AL, have an effective dose range. This suggests that even though the amount of AL delivered by the nanoadjuvants might not be enough to achieve the same level of effectiveness as the standard treatment on its own, it might offer other advantages. Particularly, the @fPD group achieved a good therapeutic effect by delivering a lower dose of AL more efficiently. This approach may widen the therapeutic window for AL, meaning it could be effective at a broader range of doses and potentially reduce side effects. In general, dose-related issues are major limitations that should be explored in gradient controlled studies in the future.

In summary, this study successfully synthesized calcium and phosphorus-incorporated fluffy hybrid nanoparticles and employed -PEG-$DAsp_8$ to achieve bone targeting modification to fabricate low-dose AL nanoadjuvants, referred to as @fPD. This fluffy @fPD promoted the cellular uptake and intracellular delivery of AL by activating the adhesion pathway via two representative adhesion proteins, namely CARD11 and CD34 molecules. Moreover, @fPD enhanced the sustained release of AL and extended its *in vivo* half-life. Consequently, low-dose therapy with @fPD effectively reversed the imbalance between osteoclastic and osteogenic niches and mitigated bone loss in osteoporosis. Our findings demonstrate a novel concept for developing a drug delivery system with enhanced bioactivity and therapeutic effect at lower administration dosages. This will expand the application of nanomaterials thereby treat osteoporosis and other bone diseases.

Funding

National Natural Science Foundation of China 82172233 (X. Y.). Shanghai Baoshan District Science and Technology Commission medical health project 21-E−52 (B. F.).

Ethics approval and consent to participate

All procedures involving the use, care, and handling of animals were carried out under the guidance and supervision of the Animal Welfare and Ethics Committee at the Shanghai Sixth People's Hospital, affiliated with the Shanghai Jiao Tong University School of Medicine (approval number 20150119-013).

CRediT authorship contribution statement

Guoyang Zhang: Writing – original draft, Methodology, Conceptualization. **Yuhao Kang:** Writing – original draft, Investigation, Data curation. **Jizhao Dong:** Writing – original draft, Investigation, Data curation. **Dingyi Shi:** Investigation. **Yu Xiang:** Investigation. **Haihan Gao:** Investigation. **Zhiqi Lin:** Investigation. **Xiaojuan Wei:** Investigation. **Ren Ding:** Investigation. **Beibei Fan:** Writing – review & editing, Supervision. **Hongmei Zhang:** Investigation. **Tonghe Zhu:** Writing – review & editing, Supervision. **Liren Wang:** Writing – review & editing, Supervision. **Xiaoyu Yan:** Writing – review & editing, Writing – original draft, Supervision, Methodology, Conceptualization.

Declaration of competing interest

The authors declare no competing financial interest.

Acknowledgements

Guoyang Zhang, Yuhao Kang, and Jizhao Dong contribute equally to this work.

Appendix A. Supplementary data

Supplementary data to this article can be found online at https://doi.org/10.1016/j.bioactmat.2024.05.037.

Supporting Information

Supporting Information is available from authors.

References

[1] N. Salari, H. Ghasemi, L. Mohammadi, M.H. Behzadi, E. Rabieenia, S. Shohaimi, M. Mohammadi, The global prevalence of osteoporosis in the world: a comprehensive systematic review and meta-analysis, J. Orthop. Surg. 16 (2021) 609, https://doi.org/10.1186/s13018-021-02772-0.

[2] Y. Gao, N. Chen, Z. Fu, Q. Zhang, Progress of Wnt signaling pathway in osteoporosis, Biomolecules 13 (2023) 483, https://doi.org/10.3390/biom13030483.

[3] I. Foessl, H.P. Dimai, B. Obermayer-Pietsch, Long-term and sequential treatment for osteoporosis, Nat. Rev. Endocrinol. 19 (2023) 520–533, https://doi.org/10.1038/s41574-023-00866-9.

[4] H.A. Fink, R. MacDonald, M.L. Forte, C.E. Rosebush, K.E. Ensrud, J.T. Schousboe, V.A. Nelson, K. Ullman, M. Butler, C.M. Olson, B.C. Taylor, M. Brasure, T.J. Wilt, Long-term drug therapy and drug Discontinuations and holidays for osteoporosis fracture prevention: a systematic review, Ann. Intern. Med. 171 (2019) 37, https://doi.org/10.7326/M19-0533.

[5] W.J. Deardorff, I. Cenzer, B. Nguyen, S.J. Lee, Time to benefit of bisphosphonate therapy for the prevention of fractures among postmenopausal women with osteoporosis: a meta-analysis of randomized clinical trials, JAMA Intern. Med. 182 (2022) 33, https://doi.org/10.1001/jamainternmed.2021.6745.

[6] R.A. Lobo, A. Gompel, Management of menopause: a view towards prevention, Lancet Diabetes Endocrinol. 10 (2022) 457–470, https://doi.org/10.1016/S2213-8587(21)00269-2.

[7] R. Eastell, T.W. O'Neill, L.C. Hofbauer, B. Langdahl, I.R. Reid, D.T. Gold, S. R. Cummings, Postmenopausal osteoporosis, Nat. Rev. Dis. Primer 2 (2016) 16069, https://doi.org/10.1038/nrdp.2016.69.

[8] M. Sharpe, S. Noble, C.M. Spencer, Alendronate: an update of its use in osteoporosis, Drugs 61 (2001) 999–1039, https://doi.org/10.2165/00003495-200161070-00010.

[9] A.G. Porras, S.D. Holland, B.J. Gertz, Pharmacokinetics of alendronate, Clin. Pharmacokinet. 36 (1999) 315–328, https://doi.org/10.2165/00003088-199936050-00002.

[10] L. Zheng, Z. Zhuang, Y. Li, T. Shi, K. Fu, W. Yan, L. Zhang, P. Wang, L. Li, Q. Jiang, Bone targeting antioxidative nano-iron oxide for treating postmenopausal osteoporosis, Bioact. Mater. 14 (2022) 250–261, https://doi.org/10.1016/j.bioactmat.2021.11.012.

[11] F.L. Lanza, R.H. Hunt, A.B.R. Thomson, J.M. Provenza, M.A. Blank, Endoscopic comparison of esophageal and gastroduodenal effects of risedronate and alendronate in postmenopausal women, Gastroenterology 119 (2000) 631–638, https://doi.org/10.1053/gast.2000.16517.

[12] D. Lin, J.R. Kramer, D. Ramsey, A. Alsarraj, G. Verstovsek, M. Rugge, P. Parente, D. Y. Graham, H.B. El-Serag, Oral bisphosphonates and the risk of Barrett's esophagus: case–control analysis of US veterans, Am. J. Gastroenterol. 108 (2013) 1576–1583, https://doi.org/10.1038/ajg.2013.222.

[13] C.E. Lowe, S.J. Vanner, J.B. Meddings, Upper Gastrointestinal Toxicity of Alendronate, 2000, p. 95.

[14] S.R. Cummings, A.C. Santora, D.M. Black, R.G.G. Russell, History of alendronate, Bone 137 (2020) 115411, https://doi.org/10.1016/j.bone.2020.115411.

[15] C. Ayers, D. Kansagara, B. Lazur, R. Fu, A. Kwon, C. Harrod, Effectiveness and safety of treatments to prevent fractures in People with low bone mass or primary osteoporosis: a living systematic review and network meta-analysis for the American college of physicians, Ann. Intern. Med. 176 (2023) 182–195, https://doi.org/10.7326/M22-0684.

[16] J. Wu, Z. Meng, A.A. Exner, X. Cai, X. Xie, B. Hu, Y. Chen, Y. Zheng, Biodegradable cascade nanocatalysts enable tumor-microenvironment remodeling for controllable CO release and targeted/synergistic cancer nanotherapy, Biomaterials 276 (2021) 121001, https://doi.org/10.1016/j.biomaterials.2021.121001.

[17] J. Wu, D.H. Bremner, S. Niu, M. Shi, H. Wang, R. Tang, L.-M. Zhu, Chemodrug-gated biodegradable hollow mesoporous organosilica nanotheranostics for multimodal imaging-guided low-temperature photothermal therapy/chemotherapy of cancer, ACS Appl. Mater. Interfaces 10 (2018) 42115–42126, https://doi.org/10.1021/acsami.8b16448.

[18] T. Sun, D. Hu, Z. Guo, H. Gong, Q. Xin, Y. Mu, J. Weng, J. Li, X. Chen, Hexapeptide decorated β-cyclodextrin delivery system for targeted therapy of bone infection, J. Controlled Release 353 (2023) 337–349, https://doi.org/10.1016/j.jconrel.2022.11.047.

[19] E. Blanco, H. Shen, M. Ferrari, Principles of nanoparticle design for overcoming biological barriers to drug delivery, Nat. Biotechnol. 33 (2015) 941–951, https://doi.org/10.1038/nbt.3330.

[20] R.K. Kankala, Y. Han, J. Na, C. Lee, Z. Sun, S. Wang, T. Kimura, Y.S. Ok, Y. Yamauchi, A. Chen, K.C.-W. Wu, Nanoarchitectured structure and surface biofunctionality of mesoporous silica nanoparticles, Adv. Mater. 32 (2020) 1907035, https://doi.org/10.1002/adma.201907035.

[21] W. Chen, C.A. Glackin, M.A. Horwitz, J.I. Zink, Nanomachines and other caps on mesoporous silica nanoparticles for drug delivery, Acc. Chem. Res. 52 (2019) 1531–1542, https://doi.org/10.1021/acs.accounts.9b00116.

[22] T.L. Nguyen, Y. Choi, J. Kim, Mesoporous silica as a versatile platform for cancer immunotherapy, Adv. Mater. 31 (2019) 1803953, https://doi.org/10.1002/adma.201803953.

[23] A. Lérida-Viso, A. Estepa-Fernández, A. García-Fernández, V. Martí-Centelles, R. Martínez-Máñez, Biosafety of mesoporous silica nanoparticles; towards clinical translation, Adv. Drug Deliv. Rev. 201 (2023) 115049, https://doi.org/10.1016/j.addr.2023.115049.

[24] Y. Zhou, G. Quan, Q. Wu, X. Zhang, B. Niu, B. Wu, Y. Huang, X. Pan, C. Wu, Mesoporous silica nanoparticles for drug and gene delivery, Acta Pharm. Sin. B 8 (2018) 165–177, https://doi.org/10.1016/j.apsb.2018.01.007.

[25] J.M. Harris, R.B. Chess, Effect of pegylation on pharmaceuticals, Nat. Rev. Drug Discov. 2 (2003) 214–221, https://doi.org/10.1038/nrd1033.

[26] S. Gupta, S. Majumdar, S. Krishnamurthy, Bioactive glass: a multifunctional delivery system, J. Controlled Release 335 (2021) 481–497, https://doi.org/10.1016/j.jconrel.2021.05.043.

[27] L. Huang, X. Mao, J. Li, Q. Li, J. Shen, M. Liu, C. Fan, Y. Tian, Nanoparticle spikes enhance cellular uptake via regulating myosin IIA recruitment, ACS Nano 17 (2023) 9155–9166, https://doi.org/10.1021/acsnano.2c12660.

[28] H. Yu, Y. Yu, R. Lin, M. Liu, Q. Zhou, M. Liu, L. Chen, W. Wang, A.A. Elzatahry, D. Zhao, X. Li, Camouflaged virus-like-nanocarrier with a transformable rough surface for boosting drug delivery, Angew. Chem. Int. Ed. 62 (2023) e202216188, https://doi.org/10.1002/anie.202216188.

[29] S. Liu, L. Zhang, Z. Li, F. Gao, Q. Zhang, A. Bianco, H. Liu, S. Ge, B. Ma, Materials-mediated in situ physical cues for bone regeneration, Adv. Funct. Mater. 34 (2024) 2306534, https://doi.org/10.1002/adfm.202306534.

[30] Q. He, Y. Gao, L. Zhang, Z. Zhang, F. Gao, X. Ji, Y. Li, J. Shi, A pH-responsive mesoporous silica nanoparticles-based multi-drug delivery system for overcoming multi-drug resistance, Biomaterials 32 (2011) 7711–7720, https://doi.org/10.1016/j.biomaterials.2011.06.066.

[31] Y. Huang, S. Nahar, M.M. Alam, S. Hu, D.W. McVicar, D. Yang, Reactive oxygen species-sensitive biodegradable mesoporous silica nanoparticles harboring TheraVac elicit tumor-specific immunity for colon tumor treatment, ACS Nano 17 (2023) 19740–19752, https://doi.org/10.1021/acsnano.3c03195.

[32] C. Huang, L. Zhang, Q. Guo, Y. Zuo, N. Wang, H. Wang, D. Kong, D. Zhu, L. Zhang, Robust nanovaccine based on polydopamine-coated mesoporous silica nanoparticles for effective photothermal-immunotherapy against melanoma, Adv. Funct. Mater. 31 (2021) 2010637, https://doi.org/10.1002/adfm.202010637.

[33] W. Wang, P. Wang, X. Tang, A.A. Elzatahry, S. Wang, D. Al-Dahyan, M. Zhao, C. Yao, C.-T. Hung, X. Zhu, T. Zhao, X. Li, F. Zhang, D. Zhao, Facile synthesis of uniform virus-like mesoporous silica nanoparticles for enhanced cellular internalization, ACS Cent. Sci. 3 (2017) 839–846, https://doi.org/10.1021/acscentsci.7b00257.

[34] S. Hu, C.C. Liu, G. Chen, T. Willett, R.N. Young, M.D. Grynpas, In vivo effects of two novel ALN-EP4a conjugate drugs on bone in the ovariectomized rat model for reversing postmenopausal bone loss, Osteoporos. Int. 27 (2016) 797–808, https://doi.org/10.1007/s00198-015-3284-x.

[35] C.C. Liu, S. Hu, G. Chen, J. Georgiou, S. Arns, N.S. Kumar, R.N. Young, M. D. Grynpas, Novel EP4 receptor agonist-bisphosphonate conjugate drug (C1) promotes bone formation and improves vertebral mechanical properties in the ovariectomized rat model of postmenopausal bone loss, J. Bone Miner. Res. 30 (2015) 670–680, https://doi.org/10.1002/jbmr.2382.

[36] M. Schumacher, P. Habibovic, S. Van Rijt, Mesoporous bioactive glass composition effects on degradation and bioactivity, Bioact. Mater. 6 (2021) 1921–1931, https://doi.org/10.1016/j.bioactmat.2020.12.007.

[37] Y.-H. Han, C.-G. Liu, B.-Q. Chen, C.-P. Fu, R.K. Kankala, S.-B. Wang, A.-Z. Chen, Orchestrated tumor apoptosis (Cu2+) and bone tissue calcification (Ca2+) by hierarchical Copper/Calcium-ensembled bioactive silica for osteosarcoma therapy, Chem. Eng. J. 435 (2022) 134820, https://doi.org/10.1016/j.cej.2022.134820.

[38] G. Miao, X. Chen, H. Dong, L. Fang, C. Mao, Y. Li, Z. Li, Q. Hu, Investigation of emulsified, acid and acid-alkali catalyzed mesoporous bioactive glass microspheres for bone regeneration and drug delivery, Mater. Sci. Eng. C 33 (2013) 4236–4243, https://doi.org/10.1016/j.msec.2013.06.022.

[39] S. Meejoo, W. Maneeprakorn, P. Winotai, Phase and thermal stability of nanocrystalline hydroxyapatite prepared via microwave heating, Thermochim. Acta 447 (2006) 115–120, https://doi.org/10.1016/j.tca.2006.04.013.

[40] S.M. Londoño-Restrepo, R. Jeronimo-Cruz, B.M. Millán-Malo, E.M. Rivera-Muñoz, M.E. Rodriguez-García, Effect of the nano crystal size on the X-ray diffraction patterns of biogenic hydroxyapatite from human, bovine, and porcine bones, Sci. Rep. 9 (2019) 5915, https://doi.org/10.1038/s41598-019-42269-9.

[41] T. Kokubo, H. Takadama, How useful is SBF in predicting in vivo bone bioactivity? Biomaterials 27 (2006) 2907–2915, https://doi.org/10.1016/j.biomaterials.2006.01.017.

[42] X. Li, L. Zhang, X. Dong, J. Liang, J. Shi, Preparation of mesoporous calcium doped silica spheres with narrow size dispersion and their drug loading and degradation behavior, Microporous Mesoporous Mater. 102 (2007) 151–158, https://doi.org/10.1016/j.micromeso.2006.12.048.

[43] C.-C. Chang, T.-A. Lin, S.-Y. Wu, C.-P. Lin, H.-H. Chang, Regeneration of tooth with allogenous, autoclaved treated dentin matrix with dental pulpal stem cells: an in vivo study, J. Endod. 46 (2020) 1256–1264, https://doi.org/10.1016/j.joen.2020.05.016.

[44] C. Shi, T. Wu, Y. He, Y. Zhang, D. Fu, Recent advances in bone-targeted therapy, Pharmacol. Ther. 207 (2020) 107473, https://doi.org/10.1016/j.pharmthera.2020.107473.

[45] J. Liu, X. Wu, J. Lu, G. Huang, L. Dang, H. Zhang, C. Zhong, Z. Zhang, D. Li, F. Li, C. Liang, Y. Yu, B.-T. Zhang, L. Chen, A. Lu, G. Zhang, Exosomal transfer of osteoclast-derived miRNAs to chondrocytes contributes to osteoarthritis progression, Nat. Aging 1 (2021) 368–384, https://doi.org/10.1038/s43587-021-00050-6.

[46] S.C. Miller, H. Pan, D. Wang, B.M. Bowman, P. Kopečková, J. Kopeček, Feasibility of using a bone-targeted, macromolecular delivery system coupled with prostaglandin E1 to promote bone formation in aged, estrogen-deficient rats, Pharm. Res. (N. Y.) 25 (2008) 2889–2895, https://doi.org/10.1007/s11095-008-9706-0.

[47] C. Xu, M. Yu, O. Noonan, J. Zhang, H. Song, H. Zhang, C. Lei, Y. Niu, X. Huang, Y. Yang, C. Yu, Core-cone structured monodispersed mesoporous silica nanoparticles with ultra-large cavity for protein delivery, Small 11 (2015) 5949–5955, https://doi.org/10.1002/smll.201501449.

[48] J. Wen, K. Yang, F. Liu, H. Li, Y. Xu, S. Sun, Diverse gatekeepers for mesoporous silica nanoparticle based drug delivery systems, Chem. Soc. Rev. 46 (2017) 6024–6045, https://doi.org/10.1039/C7CS00219J.

[49] H. Duan, J. Diao, N. Zhao, Y. Ma, Synthesis of hollow mesoporous bioactive glass microspheres with tunable shell thickness by hydrothermal-assisted self-transformation method, Mater. Lett. 167 (2016) 201–204, https://doi.org/10.1016/j.matlet.2015.12.162.

[50] J.H. Lee, I.H. Ko, S.-H. Jeon, J.-H. Chae, J.H. Chang, Micro-structured hydroxyapatite microspheres for local delivery of alendronate and BMP-2 carriers, Mater. Lett. 105 (2013) 136–139, https://doi.org/10.1016/j.matlet.2013.04.082.

[51] P. Wei, Z. Yuan, W. Jing, Y. Huang, Q. Cai, B. Guan, Z. Liu, X. Zhang, J. Mao, D. Chen, X. Yang, Strengthening the potential of biomineralized microspheres in enhancing osteogenesis via incorporating alendronate, Chem. Eng. J. 368 (2019) 577–588, https://doi.org/10.1016/j.cej.2019.02.202.

[52] E.A. Taha, N.F. Youssef, Spectrophotometric determination of some drugs for osteoporosis, Chem. Pharm. Bull. (Tokyo) 51 (2003) 1444–1447, https://doi.org/10.1248/cpb.51.1444.

[53] F. Jia, L. Ruan, C. Du, Y. Liu, X. Cai, R. Dou, J. Zhang, X. Liu, J. Chen, X. Zhang, Z. Chai, Y. Hu, The nanoformula of zoledronic acid and calcium carbonate targets osteoclasts and reverses osteoporosis, Biomaterials 296 (2023) 122059, https://doi.org/10.1016/j.biomaterials.2023.122059.

[54] Y. Liu, L. Wang, Z. Liu, Y. Kang, T. Chen, C. Xu, T. Zhu, Durable immunomodulatory nanofiber niche for the functional remodeling of cardiovascular tissue, ACS Nano 18 (2024) 951–971, https://doi.org/10.1021/acsnano.3c09692.

[55] K. Stellos, H. Langer, K. Daub, T. Schoenberger, A. Gauss, T. Geisler, B. Bigalke, I. Mueller, M. Schumm, I. Schaefer, P. Seizer, B.F. Kraemer, D. Siegel-Axel, A. E. May, S. Lindemann, M. Gawaz, Platelet-derived stromal cell–derived factor-1 regulates adhesion and promotes differentiation of human CD34 $^{+}$ cells to endothelial progenitor cells, Circulation 117 (2008) 206–215, https://doi.org/10.1161/CIRCULATIONAHA.107.714691.

[56] C. Sassetti, A. Van Zante, S.D. Rosen, Identification of endoglycan, a member of the CD34/podocalyxin family of sialomucins, J. Biol. Chem. 275 (2000) 9001–9010, https://doi.org/10.1074/jbc.275.12.9001.

[57] R. Srivastava, B.J. Burbach, Y. Shimizu, NF-κB activation in T cells requires discrete control of IκB kinase α/β (IKKα/β) phosphorylation and IKKγ ubiquitination by the ADAP adapter protein, J. Biol. Chem. 285 (2010) 11100–11105, https://doi.org/10.1074/jbc.M109.068999.

[58] E.D. Roberson, K. Scearce-Levie, J.J. Palop, F. Yan, I.H. Cheng, T. Wu, H. Gerstein, G.-Q. Yu, L. Mucke, Reducing endogenous tau ameliorates amyloid ß-induced deficits in an alzheimer's disease mouse model, Science 316 (2007) 750–754, https://doi.org/10.1126/science.1141736.

[59] N. Cirillo, S.S. Prime, Desmosomal interactome in keratinocytes: a systems biology approach leading to an understanding of the pathogenesis of skin disease, Cell. Mol. Life Sci. 66 (2009) 3517–3533, https://doi.org/10.1007/s00018-009-0139-7.

[60] P. Gosavi, S.T. Kundu, N. Khapare, L. Sehgal, M.S. Karkhanis, S.N. Dalal, E-cadherin and plakoglobin recruit plakophilin3 to the cell border to initiate desmosome assembly, Cell. Mol. Life Sci. 68 (2011) 1439–1454, https://doi.org/10.1007/s00018-010-0531-3.

[61] H. Chu, I. Thievessen, M. Sixt, T. Lammermann, A. Waisman, A. Braun, A. A. Noegel, R. Fassler, ✐-Parvin is dispensable for hematopoiesis, leukocyte trafficking, and T-cell-dependent antibody response, Mol. Cell Biol. 26 (2006), https://doi.org/10.1128/MCB.26.5.1817-1825.2006.

[62] J.G. Flanagan, D.C. Chan, H.H. Medical, Transmembrane form of the kit ligand growth factor is determined by alternative splicing and is Missing in The Nd Mutant, (n.d.)...

[63] C. Buccitelli, M. Selbach, mRNAs, proteins and the emerging principles of gene expression control, Nat. Rev. Genet. 21 (2020) 630–644, https://doi.org/10.1038/s41576-020-0258-4.

[64] R.A.B. Silva, A.P. Sousa-Pereira, M.P. Lucisano, P.C. Romualdo, F.W.G. Paula-Silva, A. Consolaro, L.A.B. Silva, P. Nelson-Filho, Alendronate inhibits osteocyte apoptosis and inflammation via IL -6, inhibiting bone resorption in periapical lesions of ovariectomized rats, Int. Endod. J. 53 (2020) 84–96, https://doi.org/10.1111/iej.13206.

[65] S. Hu, C.C. Liu, G. Chen, T. Willett, R.N. Young, M.D. Grynpas, In vivo effects of two novel ALN-EP4a conjugate drugs on bone in the ovariectomized rat model for reversing postmenopausal bone loss, Osteoporos. Int. 27 (2016) 797–808, https://doi.org/10.1007/s00198-015-3284-x.

[66] M. Neidhart, X. Baraliakos, C. Seemayer, C. Zelder, R.E. Gay, B.A. Michel, H. Boehm, S. Gay, J. Braun, Expression of cathepsin K and matrix metalloproteinase 1 indicate persistent osteodestructive activity in long-standing ankylosing spondylitis, Ann. Rheum. Dis. 68 (2009) 1334–1339, https://doi.org/10.1136/ard.2008.092494.

[67] I. Itonaga, A. Sabokbar, D.W. Murray, N.A. Athanasou, EVect of Osteoprotegerin and Osteoprotegerin Ligand on Osteoclast Formation by Arthroplasty Membrane Derived Macrophages, (n.d.)...

[68] T. Kukita, N. Wada, A. Kukita, T. Kakimoto, F. Sandra, K. Toh, K. Nagata, T. Iijima, M. Horiuchi, H. Matsusaki, K. Hieshima, O. Yoshie, H. Nomiyama, RANKL-Induced DC-STAMP is essential for Osteoclastogenesis. https://doi.org/10.1084/jem.20040518, 2004.

[69] A. Fleischmann, W. Jochum, R. Eferl, J. Witowsky, E.F. Wagner, Rhabdomyosarcoma development in mice lacking Trp53 and Fos: tumor suppression by the Fos protooncogene, Cancer Cell (2003), https://doi.org/10.1016/S1535-6108(03)00280-0.

[70] A.I. Idris, J. Rojas, I.R. Greig, R.J. Van'T Hof, S.H. Ralston, Aminobisphosphonates cause osteoblast apoptosis and inhibit bone Nodule formation in vitro, Calcif. Tissue Int. 82 (2008) 191–201, https://doi.org/10.1007/s00223-008-9104-y.

[71] E.M. Lotz, C.H. Lohmann, B.D. Boyan, Z. Schwartz, Bisphosphonates inhibit surface-mediated osteogenesis, J. Biomed. Mater. Res. 108 (2020) 1774–1786, https://doi.org/10.1002/jbm.a.36944.

[72] A. El-Fiqi, J.H. Lee, E.-J. Lee, H.-W. Kim, Collagen hydrogels incorporated with surface-aminated mesoporous nanobioactive glass: improvement of physicochemical stability and mechanical properties is effective for hard tissue engineering, Acta Biomater. 9 (2013) 9508–9521, https://doi.org/10.1016/j.actbio.2013.07.036.

[73] A. El-Fiqi, J.-H. Kim, H.-W. Kim, Osteoinductive Fibrous scaffolds of Biopolymer/mesoporous bioactive glass Nanocarriers with excellent bioactivity and long-term delivery of osteogenic drug, ACS Appl. Mater. Interfaces 7 (2015) 1140–1152, https://doi.org/10.1021/am5077759.

[74] Department of Clinical Sciences, Colorado State University, Ft. CollinsCO 80523, USA, A. Simon Turner, Animal models of osteoporosis - necessity and limitations, Eur. Cell. Mater. 1 (2001) 66–81, https://doi.org/10.22203/eCM.v001a08.

[75] N. Yousefzadeh, K. Kashfi, S. Jeddi, A. Ghasemi, Ovariectomized rat model of osteoporosis: a PRACTICAL guide, EXCLI J (2019).

[76] E.G. Colman, The food and drug Administration's osteoporosis guidance Document: Past, present, and future, J. Bone Miner. Res. 18 (2003) 1125–1128, https://doi.org/10.1359/jbmr.2003.18.6.1125.

[77] R.T. Turner, J.J. Vandersteenhoven, N.H. Bell, The effects of ovariectomy and 17β-estradiol on cortical bone histomorphometry in growing rats, J. Bone Miner. Res. 2 (1987) 115–122, https://doi.org/10.1002/jbmr.5650020206.

[78] W. Wang, P. Wang, L. Chen, M. Zhao, C.-T. Hung, C. Yu, A.A. Al-Khalaf, W. N. Hozzein, F. Zhang, X. Li, D. Zhao, Engine-trailer-Structured Nanotrucks for efficient nano-Bio interactions and Bioimaging-Guided drug delivery, Chem 6 (2020) 1097–1112, https://doi.org/10.1016/j.chempr.2020.01.010.

[79] J. Gao, Q. Song, X. Gu, G. Jiang, J. Huang, Y. Tang, R. Yu, A. Wang, Y. Huang, G. Zheng, H. Chen, X. Gao, Intracerebral fate of organic and inorganic nanoparticles is dependent on microglial extracellular vesicle function, Nat. Nanotechnol. (2023), https://doi.org/10.1038/s41565-023-01551-8.